The Discovery and Evolution of a Possible New Epoch of Cometary Activity by the Centaur (2060) Chiron

Matthew M. Dobson[1], Megan E. Schwamb[1], Alan Fitzsimmons[1], Charles Schambeau[2], Aren Beck[2], Larry Denneau[3], Nicolas Erasmus[4], A. N. Heinze[5], Luke J. Shingles[1,6], Robert J. Siverd[3], Ken W. Smith[1], John L. Tonry[3], Henry Weiland[3], David R. Young[1], Michael S. P. Kelley[7], Tim Lister[8], Pedro H. Bernardinelli[5], Marin Ferrais[9], Emmanuel Jehin[10], Grigori Fedorets[1,11,12], Susan D. Benecchi[13], Anne J. Verbiscer[14], Joseph Murtagh[1], René Duffard[15], Edward Gomez[16], Joey Chatelain[8], and Sarah Greenstreet[5,17]

[1] Astrophysics Research Centre, School of Mathematics and Physics, Queen's University Belfast, Belfast BT7 1NN, UK
[2] Florida Space Institute, University of Central Florida, 12354 Research Parkway, Partnership 1 Building, Orlando, FL 32828, USA
[3] Institute for Astronomy, University of Hawaii at Manoa, Honolulu, HI 96822, USA
[4] South African Astronomical Observatory, Cape Town 7925, South Africa
[5] Department of Astronomy and the DIRAC Institute, University of Washington, 3910 15th Avenue NE, Seattle, WA 98195, USA
[6] GSI Helmholtzzentrum für Schwerionenforschung, Planckstraße 1, 64291 Darmstadt, Germany
[7] Department of Astronomy, University of Maryland, College Park, MD 20742-0001, USA
[8] Las Cumbres Observatory, 6740 Cortona Drive, Suite 102, Goleta, CA 93117, USA
[9] Arecibo Observatory, University of Central Florida, HC-3 Box 53995, Arecibo, PR 00612, USA
[10] Space sciences, Technologies & Astrophysics Research (STAR) Institute, University of Liège, Belgium
[11] Finnish Centre for Astronomy with ESO, University of Turku, FI-20014 Turku, Finland
[12] Department of Physics, P.O. Box 64, FI-00014 University of Helsinki, Finland
[13] Planetary Science Institute, 1700 East Fort Lowell Road, Suite 106, Tucson, AZ 85719, USA
[14] Department of Astronomy, University of Virginia, P.O. Box 400325, Charlottesville, VA 22904-4325, USA
[15] Instituto de Astrofísica de Andalucía—CSIC. Glorieta de la Astronomía s/n. Granada, Spain
[16] Las Cumbres Observatory, School of Physics and Astronomy, Cardiff University, Queens Buildings, The Parade, Cardiff CF24 3AA, UK
[17] Rubin Observatory/NSF's NOIRLab, 950 North Cherry Avenue, Tucson, AZ 85719, USA

Abstract

Centaurs are small solar system objects on chaotic orbits in the giant planet region, forming an evolutionary continuum with the Kuiper Belt objects and Jupiter-family comets. Some Centaurs are known to exhibit cometary activity, though unlike comets, this activity tends not to correlate with heliocentric distance, and the mechanism behind it is currently poorly understood. We utilize serendipitous observations from the Asteroid Terrestrial-impact Last Alert System, Zwicky Transient Facility, Panoramic Survey Telescope and Rapid Response System, Dark Energy Survey, and Gaia in addition to targeted follow-up observations from the Las Cumbres Observatory, TRAnsiting Planets and PlanetesImals Small Telescope South (TRAPPIST-South), and Gemini North telescope to analyze an unexpected brightening exhibited by the known active Centaur (2060) Chiron in 2021. This is highly indicative of a cometary outburst. As of 2023 February, Chiron had still not returned to its prebrightening magnitude. We find Chiron's rotational lightcurve, phase curve effects, and possible high-albedo surface features to be unlikely causes of this observed brightening. We consider the most likely cause to be an epoch of either new or increased cometary activity, though we cannot rule out a possible contribution from Chiron's reported ring system, such as a collision of as-yet-unseen satellites shepherding the rings. We find no evidence for a coma in our Gemini or TRAPPIST-South observations, though this does not preclude the possibility that Chiron is exhibiting a coma that is too faint for observation or constrained to the immediate vicinity of the nucleus.

1. Introduction

The Centaurs are small icy objects residing on dynamically unstable orbits in the giant planet region of the solar system. Centaurs are thought to originate as primordial Kuiper Belt objects (KBOs) on Neptune-crossing orbits that are then scattered by Neptune into the giant planet region (Duncan & Levison 1997; Levison & Duncan 1997; Volk & Malhotra 2008), where they reside on chaotic orbits with an average orbital lifetime of the order of $\sim 10^6$–10^8 yr (Hahn & Bailey 1990; Tiscareno & Malhotra 2003; Di Sisto & Brunini 2007; Volk & Malhotra 2008; Bailey & Malhotra 2009). During this time, Centaurs undergo encounters with the giant planets, causing the Centaurs to either impact the giant planets, be ejected out of the solar system altogether, or become short-period comets that include the Jupiter-family comets (JFCs; Tiscareno & Malhotra 2003; Duncan et al. 2004; Bauer et al. 2013; Fernández et al. 2013; Sarid et al. 2019). Centaurs thus form an evolutionary link between the Kuiper Belt and the more physically evolved JFCs, and this intermediate transitionary nature makes them valuable in studying the evolution of JFCs.

Approximately 8%–10% of Centaurs are known to exhibit dust comae, indicating cometary activity (Peixinho et al. 2020). However, for most active Centaurs, especially those with large perihelia, their activity differs from that of JFCs in that it occurs throughout their orbits (Peixinho et al. 2020). Centaur activity appears to be dependent on a Centaur's perihelion distance from the Sun, with a possible boundary existing at ∼14 au beyond which no activity has been detected (Jewitt 2009, 2015; Guilbert-Lepoutre 2012; Li et al. 2020; Lilly et al. 2021, 2024). The mechanism behind this phenomenon currently remains unknown, with newly exposed pockets of volatile surface ices (Prialnik 1992) as well as volatiles released during the amorphous-to-crystalline transition of subsurface ice (Jewitt 2009) being proposed to explain Centaur activity. Known active Centaurs tend to reside in orbits with smaller semimajor axes than inactive ones (Jewitt 2009) with active Centaurs tending to have experienced recent ($\sim10^2$–10^3 yr) dynamical encounters with the giant planets, causing a significant decrease in their semimajor axes (Fernández et al. 2018; Lilly et al. 2021, 2024). Combined with the comparative lack of planetary encounters experienced by inactive Centaurs, this hints that a sudden decrease in perihelia could trigger the onset of Centaur activity (Fernández et al. 2018; Lilly et al. 2021, 2024).

(2060) 95P/Chiron (henceforth Chiron) is one of the largest members of the Centaur population and has a well-established history of cometary activity (Tholen et al. 1988; Bus et al. 1989; Meech & Belton 1989; Dahlgren et al. 1990; Hartmann et al. 1990; Luu & Jewitt 1990; Meech & Belton 1990; Meech 1990; West 1990; Buratti & Dunbar 1991; Dahlgren et al. 1991; Sykes & Walker 1991; West 1991; Buie et al. 1993; Luu 1993; Marcialis & Buratti 1993; Elliot et al. 1995; Bus et al. 1996, 2001; Lazzaro et al. 1996, 1997; Silva & Cellone 2001; Belskaya et al. 2010). Cometary activity was first discovered in 1989 when a coma was detected around Chiron as it approached perihelion (Meech & Belton 1989; Hartmann et al. 1990; Meech 1990) and remained detectable even when the absolute magnitude of Chiron was at its dimmest recorded value near perihelion (Silva & Cellone 2001). Subsequent analysis of archival photographic plates obtained from 1969 to 1977 has also revealed that Chiron was active near aphelion (Bus et al. 2001). This cometary activity is thought to contribute to the considerable variation in the brightness of Chiron observed over time (Bus et al. 2001; Duffard et al. 2002; Belskaya et al. 2010). Models of Chiron's nucleus and reported ring system require a contribution from cometary outbursts to reproduce Chiron's measured lightcurve (Ortiz et al. 2015).

Between 2021 February and 2021 June, Chiron underwent a sudden brightening in apparent magnitude by ∼1 mag, remaining brighter than previous years for all of its 2021–2022 observing season (Dobson et al. 2021; Betzler 2023; Dobson et al. 2023; Ortiz et al. 2023), potentially indicative of an epoch of either new or increased cometary activity (Dobson et al. 2021, 2023; Ortiz et al. 2023). We refer to this observed brightening as the 2021 Brightening Event hereafter. In this paper, we analyze the 2021 Brightening Event exhibited by Chiron. We utilize multiwavelength photometry from the Asteroid Terrestrial-impact Last Alert System (ATLAS; Tonry et al. 2018a, 2018b), the Zwicky Transient Facility (ZTF; Bellm et al. 2019; Graham et al. 2019), and the Panoramic Survey Telescope and Rapid Response System (Pan-STARRS; Kaiser et al. 2002; Hodapp et al. 2004; Kaiser 2004; Denneau et al. 2013; Chambers et al. 2016; Magnier et al.

2020a, 2020b, 2020c; Flewelling et al. 2020; Waters et al. 2020) spanning multiple observing seasons, in addition to follow-up photometric observations taken by the 8.1 m telescope of the Gemini Observatory (Hook et al. 2004; Gimeno et al. 2016) and the Las Cumbres Observatory (LCO) telescope network (Brown et al. 2013) via the LCO Outbursting Objects Key (LOOK) project (Lister et al. 2022). We further supplement our data set with observations from the Gaia Data Release 3 (DR3; Gaia Collaboration et al. 2023; Tanga et al. 2023), the robotic TRAnsiting Planets and PlanetesImals Small Telescope South (TRAPPIST-South; Jehin et al. 2011), the Dark Energy Survey (DES; The Dark Energy Survey Collaboration 2005), and observations of Chiron reported in the literature. Our paper is structured as follows. In Section 2, we present details of the photometry used in this study and the data reduction techniques used for each data set. We present our methods of analyzing our observations in Section 3. In Section 4, we present our results of analyzing the 2021 Brightening Event for photometric behavior, color change, the search for a coma, and determining the contribution from Chiron's reported ring system. We discuss the results of our analysis and their implications for the cause of the 2021 Brightening Event in Section 5. We list the conclusions of our study in Section 6.

2. Observations and Data Reduction

This section briefly summarizes each telescope and/or survey and describes the observations we use in our analysis. Our data set is comprised of targeted observations (TRAPPIST-South, Gemini, and LOOK) and survey observations (Pan-STARRS, DES, Gaia, ATLAS, and ZTF) where Chiron was serendipitously imaged. Our observations range in time from 2012 to 2023, sampling Chiron's lightcurve pre-, during, and post-2021 Brightening Event. Tables of all observations from each telescope/survey are listed in the Appendix, with the number of observations in each filter from each telescope/survey listed in Table 1. Most of our observations are from the ATLAS data set, followed by ZTF, and the combined ATLAS and ZTF cover the largest time span in our sample. These large data sets therefore constitute the majority of our analysis. Pan-STARRS provides our earliest consistent observations of Chiron, extending our baseline to 2009. Our observations from Gemini occurred just after the 2021 Brightening Event and allow us to search for any coma exhibited by Chiron during this time. Our observations span 12 observing seasons when Chiron's on-sky distance from the Sun was sufficient to allow observations. The date ranges of each observing season are listed in Table 2. For clarity, we designate each observing season with a letter as described in Table 2.

2.1. ATLAS

ATLAS consists of four 0.5 m Schmidt telescopes at sites in Hawai'i, Chile, and South Africa, each covering a 28.9 deg^2 field of view per exposure (Tonry et al. 2018a, 2018b). ATLAS regularly observes the sky to a limiting magnitude of ∼19.5 mag in two nonstandard wideband filters, cyan (c, spanning 420–650 nm) and orange (o, spanning 560–820 nm). Further details of the ATLAS system and data reduction pipeline are described in Tonry et al. (2018a, 2018b) and Smith et al. (2020). We utilize serendipitous observations from all four ATLAS telescope sites, obtaining our magnitude measurements of Chiron via the ATLAS

<div align="center">

Table 1
Number and Time Ranges of Observations of Chiron for Each Filter of Each Telescope/Survey

</div>

Telescope/Survey	Filter	Start Date (YYYY-MM-DD)	End Date (YYYY-MM-DD)	Number of Observations
Pan-STARRS	g	2010-09-05	2013-08-07	8
Pan-STARRS	r	2010-08-31	2013-08-17	11
Pan-STARRS	i	2010-09-02	2014-10-11	12
Pan-STARRS	z	2010-06-22	2014-07-03	12
Pan-STARRS	y	2009-06-10	2013-10-30	12
TRAPPIST-South	B	2012-05-16	2012-09-12	8
TRAPPIST-South	V	2012-05-16	2012-09-12	9
TRAPPIST-South	R	2012-05-16	2015-09-18	82
DES	DES g	2013-09-11	2016-10-05	5
DES	DES r	2015-10-31	2016-10-05	3
DES	DES i	2015-10-31	2017-11-08	4
DES	DES z	2016-09-30	2017-11-24	4
DES	DES Y	2014-10-28	2016-11-04	3
Gaia	Gaia G	2014-10-31	2017-05-24	155
ATLAS	c	2015-08-12	2022-12-17	399
ATLAS	o	2015-07-26	2023-01-20	1369
ZTF	ZTF g	2019-11-02	2023-01-07	89
ZTF	ZTF r	2019-11-02	2023-01-12	103
Gemini	SDSS g'	2021-08-20	2022-08-02	5
Gemini	SDSS r'	2021-08-20	2022-08-02	3
Gemini	SDSS i'	2021-08-20	2022-08-02	4
LOOK	LOOK w	2021-09-06	2021-09-06	4
LOOK	SDSS g'	2022-09-04	2023-02-05	22
LOOK	SDSS r'	2022-09-04	2023-02-05	21

<div align="center">

Table 2
Date Ranges and Survey Coverage of Each Observing Season of Chiron

</div>

Observing Season	UT Start Date of Data Coverage (YYYY-MM-DD)	UT End Date of Data Coverage (YYYY-MM-DD)	Telescope/Survey Data Coverage
A	2009-06-10	2009-06-10	Pan-STARRS
B	2010-05-29	2010-11-02	Pan-STARRS
C	2011-06-17	2011-10-13	Pan-STARRS
D	2012-05-16	2012-11-16	Pan-STARRS, TRAPPIST-South
E	2013-05-16	2013-10-30	DES, Pan-STARRS, TRAPPIST-South
F	2014-07-03	2014-12-19	DES, Gaia, Pan-STARRS, TRAPPIST-South
G	2015-05-03	2015-12-30	ATLAS, DES, Gaia, TRAPPIST-South
H	2016-05-13	2017-01-09	ATLAS, Gaia, DES
I	2017-05-24	2018-01-17	ATLAS, Gaia, DES
J	2018-06-28	2019-01-24	ATLAS
K	2019-05-26	2020-01-31	ATLAS, ZTF
L	2020-05-19	2021-02-06	ATLAS, ZTF
M	2021-06-17	2022-01-20	ATLAS, Gemini, ZTF
N	2022-06-24	2023-02-05	ATLAS, Gemini, LOOK, ZTF

Note. Observing seasons A–L are before the 2021 Brightening Event, which occurred during observing season M. Observing season N is after the 2021 Brightening Event.

Forced Photometry Server[18] (Shingles et al. 2021), which fits a point-spread function (PSF) at a given object's position on the image as predicted from its orbital ephemeris cataloged by the Minor Planet Center and calculates the AB magnitude of the flux at that point. We chose to use difference images generated from the ATLAS data reduction pipeline (Tonry et al. 2018a, 2018b) instead of reduced images to reduce the effect of contaminating background stars and galaxies on the brightness measurements of Chiron. We select all ATLAS data up to and including 2023 January 20, corresponding to the most recent observation of Chiron's observing season from 2022 to 2023. From these, we select for analysis all ATLAS observations with apparent magnitudes brighter than both (i) the 5σ limiting magnitude of the image and (ii) the 3σ upper magnitude limit derived from the flux uncertainty, to ensure all measurements are from good-quality observations. All ATLAS data used for our analysis extend from 2015 July 26 to 2023 January 20. The majority of these data came from the telescopes at the two Hawai'ian sites, with contributions from all four telescopes from 2022 July 31 onward. All ATLAS data used for our analysis are listed in Table A1.

2.2. ZTF

The ZTF (Bellm et al. 2019; Graham et al. 2019) is a wide-field time-domain sky survey (Graham et al. 2019) utilizing the 48 inch (1.2 m) Samuel Oschin Schmidt Telescope at the Palomar Observatory with a 43 deg^2 field of view. Observations have been collected since 2017 October to a limiting magnitude of ~20.5 mag with 30 s exposures. Further details of ZTF and its setup and survey strategy are described in Bellm et al. (2019) and Graham et al. (2019). ZTF has accumulated photometry of Chiron in the $ZTF-g$ and $ZTF-r$ bands, extending in time from 2019 November 2 to 2023 January 12. We obtain magnitude measurements from these serendipitous observations using the FINK[19] community broker (Möller et al.

---

[18] https://fallingstar-data.com/forcedphot/

[19] https://fink-portal.org

2021), which processes all alerts of detections by ZTF and links them to the corresponding known solar system objects. Table A2 lists the magnitude values obtained via PSF photometry for all ZTF observations of Chiron used in this work.

2.3. Pan-STARRS

Pan-STARRS (Kaiser et al. 2002; Hodapp et al. 2004; Kaiser 2004; Denneau et al. 2013; Chambers et al. 2016; Magnier et al. 2020a, 2020b, 2020c; Flewelling et al. 2020; Waters et al. 2020) consists of two 1.8 m telescopes located at Haleakala Observatory, Hawai'i, observing the entire visible sky in six broadband filters, g, r, i, z, y, and w, to a limiting magnitude of $r \sim 21.2$ mag. Each telescope has a ~ 7 deg^2 field of view and is equipped with a 1.4 gigapixel camera, resulting in a $0\rlap{.}''26$ pixel resolution (Denneau et al. 2013). Further details of Pan-STARRS and its design, survey strategy, and data analysis are described in Chambers et al. (2016), Magnier et al. (2020a, 2020b, 2020c), Waters et al. (2020), and Flewelling et al. (2020). Throughout its observation baseline, Pan-STARRS has obtained serendipitous observations of Chiron in the g, r, i, z, and y filters, ranging in time from 2009 June 10 to 2014 October 11. We utilize the Canadian Astronomy Data Center solar system Object Image Search[20] (Gwyn et al. 2012) to obtain magnitude measurements of Chiron from these observations, utilizing the Catalog Archive Server Jobs System,[21] developed by the Johns Hopkins University/Sloan Digital Sky Survey (SDSS) team, to query the photometry. Table A3 lists all the Pan-STARRS magnitude values from PSF photometry of Chiron used in this work.

2.4. DES

We use the public images from DES (The Dark Energy Survey Collaboration 2005) Data Release 2 (Abbott et al. 2021). DES is an imaging survey utilizing the 570 MPix Dark Energy Camera (Flaugher et al. 2015) of the 4 m Blanco telescope at the Cerro Tololo Inter-American Observatory. DES serendipitously observed Chiron during its operations between 2013 and 2019 (Bernardinelli et al. 2020; Bernardinelli & Dark Energy survey 2022; Bernardinelli et al. 2022, 2023). The Chiron images used in this work were processed using the scene-modeling photometry method of Bernardinelli et al. (2023). In addition to the photometric uncertainty derived from the scene-modeling procedure, an additional 3 mmag uncertainty was added in quadrature to account for the known scatter in the DES calibration with respect to Gaia (Abbott et al. 2021). The resulting magnitude values from PSF photometry are listed in Table A4.

2.5. Gaia

We include in our analysis serendipitous observations of Chiron from Gaia DR3 (Gaia Collaboration et al. 2016, 2018, 2023; Tanga et al. 2023) in Table A5. These observations obtained from the space-based Gaia telescope span from 2014 October 31 to 2017 May 24 in the visible white-light G-band filter (wavelength range 330–1050 nm; Jordi et al. 2010).

2.6. LOOK

The LCO operates 25 telescopes across the globe (Brown et al. 2013). As part of the LOOK project (Lister et al. 2022), we observed Chiron from 2022 September 18 to 2023 February 6 using the 13 1 m telescopes of the LCO network in Pan-STARRS g' and r' filters (Chambers et al. 2016), utilizing the NEOExchange web portal (Lister et al. 2021) to schedule our targeted observations. Each 1 m telescope utilizes a Sinistro imager comprising a Fairchild 4096×4096 pixel CCD and an Archon controller, giving a field of view of $26\rlap{.}'6 \times 26\rlap{.}'6$ with a resolution of $0\rlap{.}''387$ pixel^{-1} (Brown et al. 2013). We also include the targeted observations from Dobson et al. (2021) taken in the w band (equivalent to $g' + r' + i'$ band) on 2021 September 6. All observations were obtained with the telescope in half-rate tracking mode, with exposure times ranging from 180 to 245 s ensuring negligible on-sky motion of Chiron. These observations are automatically processed using the LCO image processing pipeline "Beautiful Algorithm to Normalize Zillions of Astronomical Images" (BANZAI; McCully et al. 2018) and automatically calibrated to the Pan-STARRS1 photometric system (Tonry et al. 2012) using the ATLAS-RefCat2 all-sky photometric catalog (Tonry et al. 2018b), the CALVIACAT software (Kelley & Lister 2021), and background field stars measured with BANZAI (Lister et al. 2022). We apply aperture photometry to the processed images utilizing a $5''$ aperture radius to all observations with seeing $\leqslant 5''$. The resulting magnitude values of each targeted observation and their associated conditions are listed in Table A6.

2.7. TRAPPIST-South

We also include targeted observations of Chiron acquired between 2012 and 2015 with TRAPPIST-South (Jehin et al. 2011), located at the La Silla Observatory in Chile at the European Southern Observatory. TRAPPIST-South is a 0.6 m Ritchey–Chrétien telescope with a thermoelectrically cooled FLI ProLine 3041-BB CCD camera providing a field of view of $22' \times 22'$ and a sampling of $1\rlap{.}''2$ pixel^{-1} in the 2×2 binned mode. The data were reduced using the PHOTOMETRYPIPE-LINE (Mommert 2017) with photometric apertures with radii of 4 pixels and calibrated to the band in which they were observed (Johnson–Cousins B, V, and R) using the Pan-STARRS catalog (Chambers et al. 2016; Magnier et al. 2020a; Flewelling et al. 2020). Table A7 lists all the data from TRAPPIST-South used for our analysis.

2.8. Gemini

We obtained g-, r-, and i-band photometry of Chiron via targeted observations taken with the Gemini Observatory from the program GN-2021B-FT-114 and through observations acquired through the Gemini Large and Long Program "Investigating the Activity Drivers of Small Bodies in the Centaur-to-Jupiter-Family Transition" (programs GN-2021B-LP-203, GN-2022A-LP-203, and GN-2022B-LP-203). Chiron data were obtained from the 8.1 m Gemini North telescope in Hawai'i using the Gemini Multi-Object Spectrograph (GMOS; Hook et al. 2004; Gimeno et al. 2016) in imaging mode. GMOS-N has a field of view of $5.5' \times 5.5'$ with a pixel resolution of $0\rlap{.}''1614$ pixel^{-1} with 2×2 binning. Observations were made in the g, r, and i bands at five epochs (2021 August 8, 2021 November 3, 2021 December 9, 2022 June 24, and 2022 August 2) with all observations sidereally tracked. The

exposure times of each individual observation in a sequence were short enough that Chiron's on-sky motion (maximum $5''.53 \, hr^{-1}$) would be negligible at the 2×2 binned pixel scale, ensuring a symmetric PSF. Table A8 provides details of the observing circumstances for all our observing sequences of Chiron with Gemini. All Gemini GMOS images were reduced, including bias subtraction, flat-field correction, and mosaicking of the three CCD images, using the Gemini Data Reduction for Astronomy from Gemini Observatory North and South (DRAGONS) Python package (Labrie et al. 2019, 2023). Individual images were then processed using our custom Python-based GMOS reduction and calibration pipeline. The pipeline includes (1) cosmic-ray removal performed utilizing the LACosmic technique (van Dokkum 2001) as implemented in ccdproc (Craig et al. 2017; McCully et al. 2018), (2) stacking of individual images in Chiron's nonsidereal frame and the sidereal frame, and (3) a Pan-STARRS-based calibration using field stars from the GMOS field of view stacked in the sidereal frame, utilizing their catalog magnitudes as archived in the PS1 MeanObject tables from the Pan-STARRS Data Release 2 (Flewelling et al. 2020; Chambers et al. 2016; Magnier et al. 2020a). We utilized SExtractor Python (Bertin & Arnouts 1996; Barbary 2016) to detect background stellar sources in our Gemini observations.

3. Data Analysis

For all our observations, we correct the time of observation for light travel time and calculate reduced magnitudes (the apparent magnitude scaled to a geocentric distance and heliocentric distance of 1 au) and their associated uncertainties, assuming negligible contribution from heliocentric and geocentric distances (obtained from JPL Horizons[22]) to the errors. To help remove any stellar contamination or spurious data points from our analysis, we split our observations into pre- and post-2021 Brightening Event. We treat each filter of each data set individually. For data sets with <50 observations—namely, DES, Gemini, Pan-STARRS, and LOOK in all filters and TRAPPIST-South in the B and V filters—we visually inspect each image, removing any observations that exhibit evidence of contamination from background sources. To remove possibly spurious data points for data sets with ⩾50 observations, we followed the prescription (Dobson et al. 2023) of removing data points with large magnitude uncertainties and σ-clipping our data set.

All observations of Chiron pre-2021 Brightening Event, corresponding to observing seasons A–L (2009–2021), are consistent with a single phase curve slope. Analyzing ATLAS and ZTF observations, which constitute the majority of our data and span observing seasons G–L (2015–2021), utilizing the same method as Dobson et al. (2023), we find that their reduced magnitude values in a given filter all reside on a single phase curve profile (see Figure 6 in Section 4.1 for more details). Therefore, we treat all observing seasons pre-2021 Brightening Event as one. From this time range, we remove all observations with magnitude uncertainties exceeding the 85th percentile of the magnitude uncertainty distribution for ATLAS and TRAPPIST-South in the R filter and 95th percentile for ZTF and Gaia. For each filter in our ATLAS, ZTF, TRAPPIST-South R, and Gaia data sets, we 3σ-clip the remaining observations to eliminate outliers in reduced magnitude.

For all observations post-2021 Brightening Event, we treat each observing season separately due to Chiron's evolving phase curve (see Section 4 for more details). We utilize the 95th percentile of the magnitude uncertainty distribution as the cutoff for our ATLAS and ZTF data sets. For a given observing season, we bin all remaining observations into two bins of phase angle, each of width equal to half the maximum phase angle span of the data set. This ensures that the algorithm does not remove features of the phase curve (e.g., opposition effect) that may not be fully sampled by the data set of one observing season. For each observing season, we 3σ-clip the observations in each bin. The comparatively smaller sizes of the Gemini and LOOK data sets means we instead manually remove any outliers caused by contamination from background sources in the images.

4. Results

In this section, we analyze the 2021 Brightening Event and its subsequent evolution to explore the potential causes of Chiron's enhanced brightness in all filters. There are several possible explanations for the 2021 Brightening Event that we test with our data set. Cometary activity could cause Chiron to increase in brightness. Chiron is a known active object with previous instances of the Centaur brightening coinciding with detections of a visible coma and/or significant PSF extension (Tholen et al. 1988; Bus et al. 1989; Meech & Belton 1989; Dahlgren et al. 1990; Hartmann et al. 1990; Luu & Jewitt 1990; Meech & Belton 1990; Meech 1990; West 1990; Bus et al. 2001; Silva & Cellone 2001). Alternatively, Chiron's ring system may instead offer an explanation for the 2021 Brightening Event. Occultation studies have revealed Chiron to be surrounded by either symmetric shell-like structures (Ruprecht et al. 2015) or a system of debris rings (Ortiz et al. 2015, 2023). Ortiz et al. (2015) found that by modeling the contribution of rings to the Centaur's absolute magnitude across its orbit, their changing orientation as viewed from Earth could explain previous instances of brightening by Chiron. Betzler (2023) hypothesized that the 2021 Brightening Event could instead be caused by variation in Chiron's surface albedo, with the seasonal appearance of a high-albedo surface feature causing the Centaur to brighten. We explore the brightness evolution and phase curve of Chiron pre-, during, and post-2021 Brightening Event (Section 4.1); search for significant changes in color index across time (Section 4.2); search for a visible coma or PSF extension in our observations (Section 4.3); and compute the effect of Chiron's ring system on its brightness evolution across our baseline of observations (Section 4.4).

4.1. Brightness Evolution

We first look at ATLAS and ZTF observations because they comprise the largest two data sets in our sample and cover the widest time span. Figure 1 plots our ATLAS and ZTF reduced magnitudes versus time, both as measured in each filter and corrected for wavelength to the ATLAS c and o filters (due to them having the largest numbers of observations) using Chiron's pre-Brightening Event $c - g$ and $o - r$ color indices calculated from the absolute magnitude values of Chiron in each filter. The reduced magnitudes separated by both survey and filter are shown in Figures 2 (panels (a) and (c)) and 3 (panels (a) and (c)). The "seesaw" motion of Chiron's

---

[22] https://ssd.jpl.nasa.gov
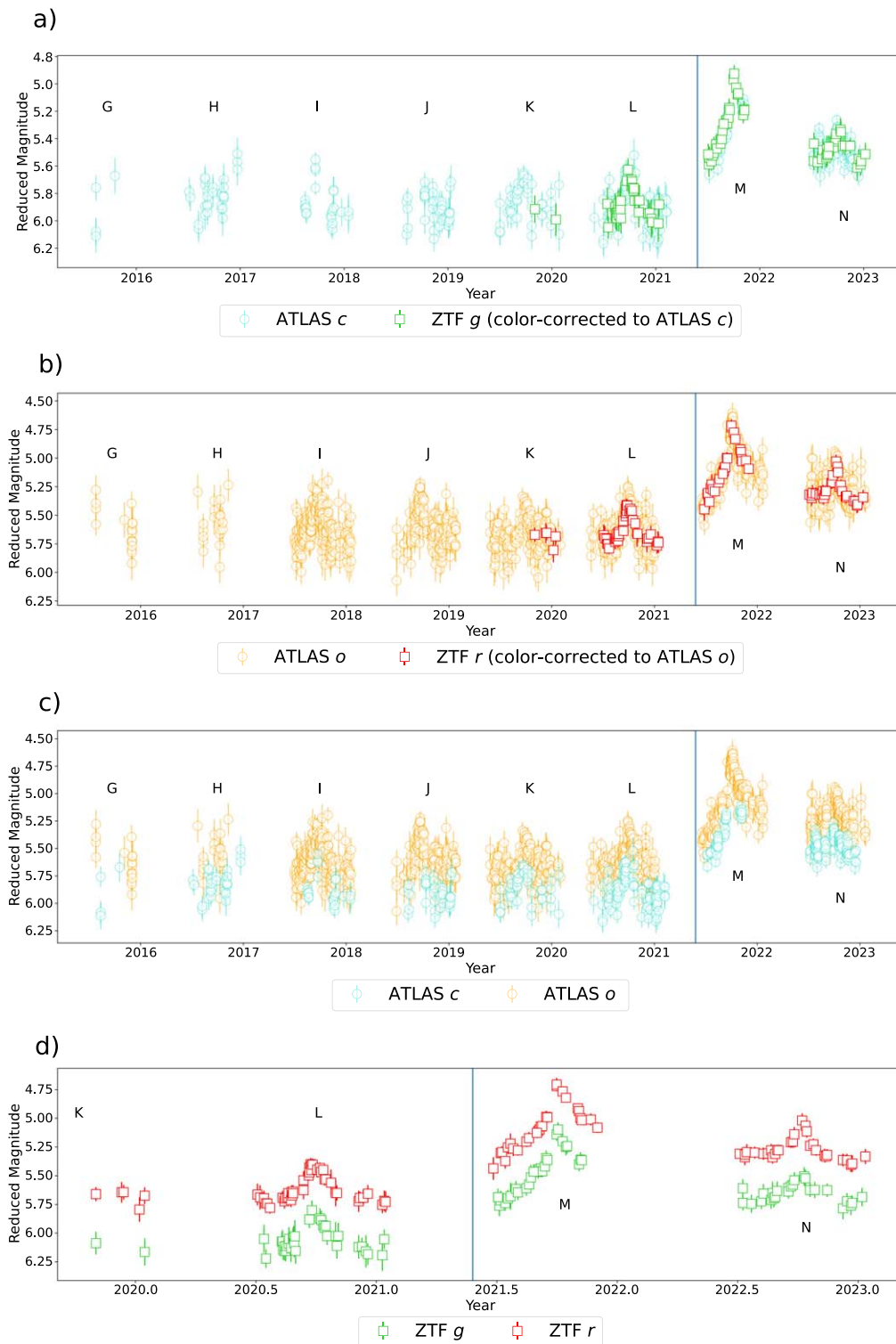
Figure 1. (a) Color-corrected reduced magnitudes vs. time of Chiron in ATLAS *c* and ZTF *g* filters. (b) Color-corrected reduced magnitudes vs. time of Chiron in ATLAS *o* and ZTF *r* filters. (c) ATLAS reduced magnitude values vs. time. (d) ZTF reduced magnitude values vs. time. Error bars are 1σ uncertainties. Note that the ATLAS and ZTF reduced magnitudes are not color-corrected in this figure. All observing seasons are labeled as per Table 2. The earliest data in this plot start at observing season G (2015–2016), as observing seasons A–F (2012–2014) have insufficient data to fully sample Chiron's brightness across time. Vertical blue lines indicate the time at which Chiron was at aphelion.

brightness over time in each observing season is due to phase curve effects, with the brightness maxima corresponding to the smallest phase angles, and the spread of the data is partly due to the periodic brightness variation caused by the Centaur's rotational lightcurve of amplitude $\Delta m \lesssim 0.1$ mag (Bus et al.

1989; Groussin et al. 2004; Ortiz et al. 2015; Cikota et al. 2018). As seen in Figure 1, Chiron's brightness varies due to phase angle by approximately the same amount across observing seasons G–L (2015–2021), with peak reduced magnitude values in each filter consistent between observing
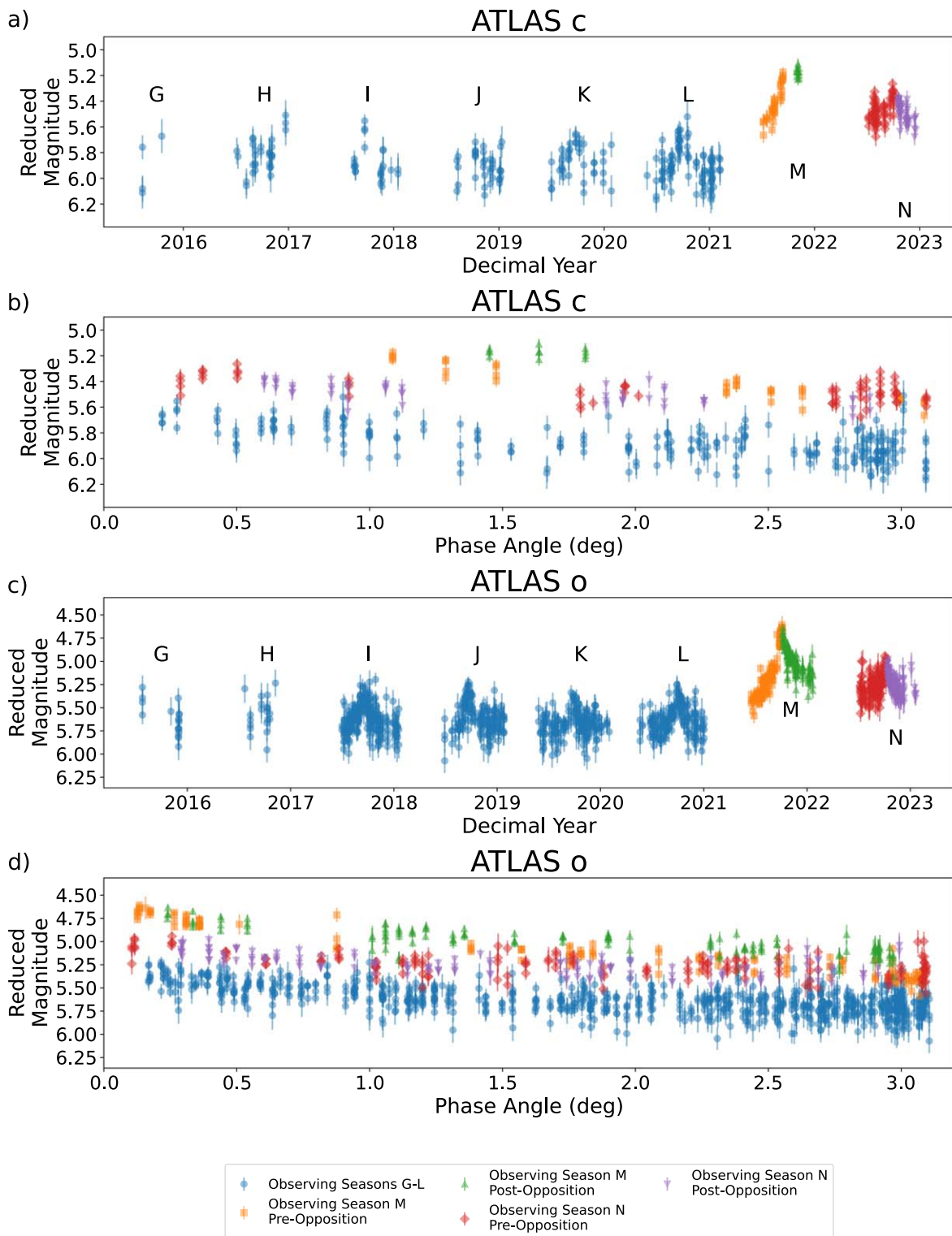
Figure 2. (a): ATLAS *c*-filter lightcurve of Chiron. (b): ATLAS *c*-filter phase curve of Chiron. (c): ATLAS *o*-filter lightcurve of Chiron. (d): ATLAS *o*-filter phase curve of Chiron. The 1σ uncertainty error bars are plotted but may be smaller than the plot markers. All observing seasons are labeled as per Table 2.

seasons. These reduced magnitude values are plotted against phase angle in Figure 4. Fitting the phase curve of Chiron in each of these observing seasons separately, we find that Chiron's phase coefficient β is consistent between observing seasons, implying that Chiron's phase curve profile had been constant before the 2021 Brightening Event (see Section 4.1.1 for more details). However, in observing season M

(2021–2022), corresponding to the 2021 Brightening Event, Chiron suddenly increases in brightness by ∼1 mag compared to all previous observing seasons. The ATLAS and ZTF observations allow us to constrain the start date of the 2021 Brightening Event to between 2021 February 6 and 2021 June 17. Chiron passed aphelion between these dates, though observations were precluded due to the Centaur being behind
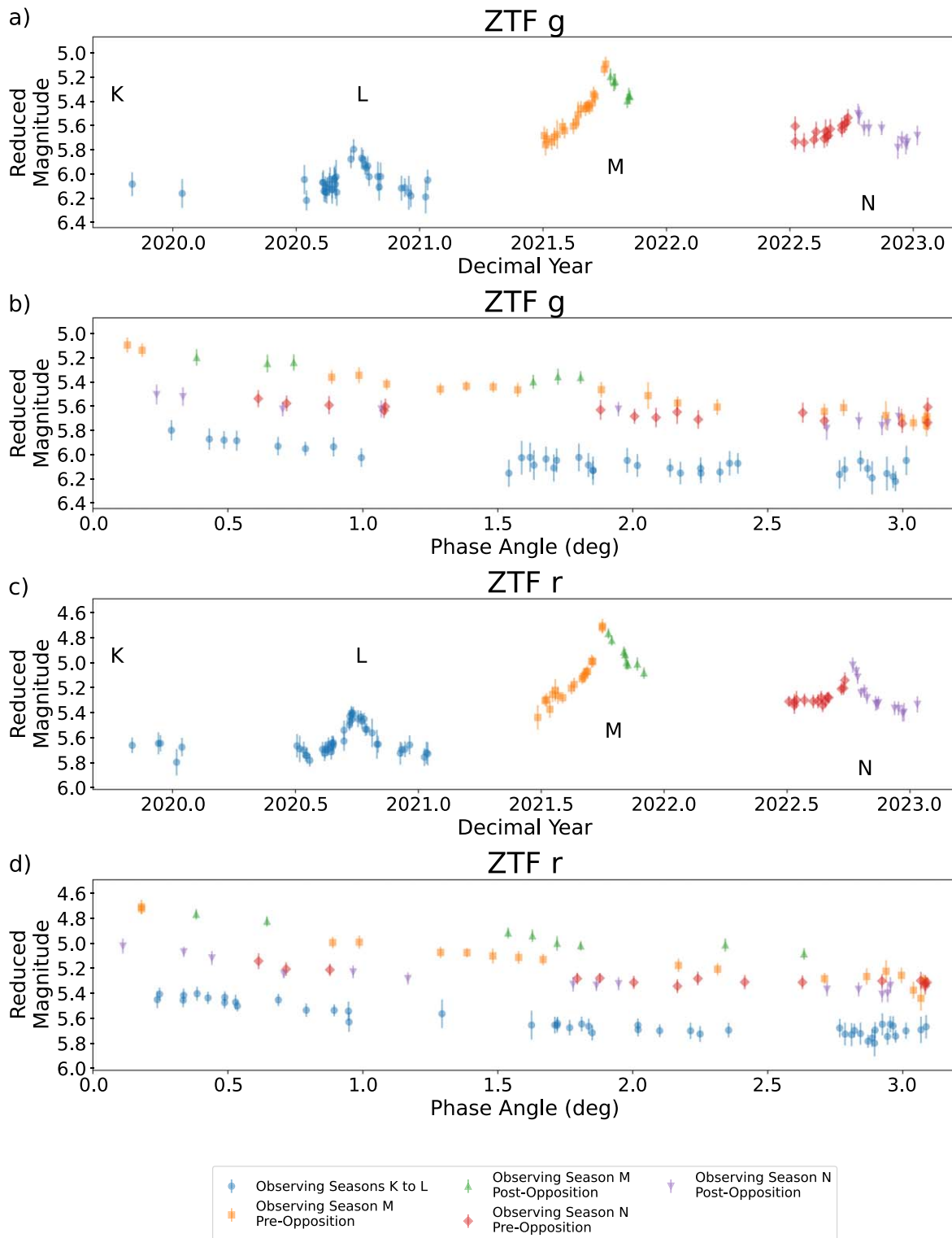
Figure 3. (a): ZTF *g*-filter lightcurve of Chiron. (b): ZTF *g*-filter phase curve of Chiron. (c): ZTF *r*-filter lightcurve of Chiron. (d): ZTF *r*-filter phase curve of Chiron. All plots are color-coded the same as Figure 2. The 1σ uncertainty error bars are plotted but may be smaller than the plot markers. All observing seasons are labeled as per Table 2.

the Sun as viewed from Earth. This observed brightness increase far exceeds Chiron's brightness variation due to rotational modulation ($\lesssim$0.1 mag) and solar phase angle ($\sim$0.5 mag), meaning that neither Chiron's lightcurve nor its phase curve can account for it. Furthermore, Chiron's brightness has continued to evolve. We see from Figure 1 that

Chiron's peak magnitude dimmed significantly by $\sim$0.5 mag between observing seasons M (2021–2022) and N (2022–2023), but it continues to remain at brighter magnitudes than compared to G–L (2015–2021) by $\sim$0.5 mag.

The phenomenon that caused the 2021 Brightening Event changed Chiron's phase curve profile as well as its absolute
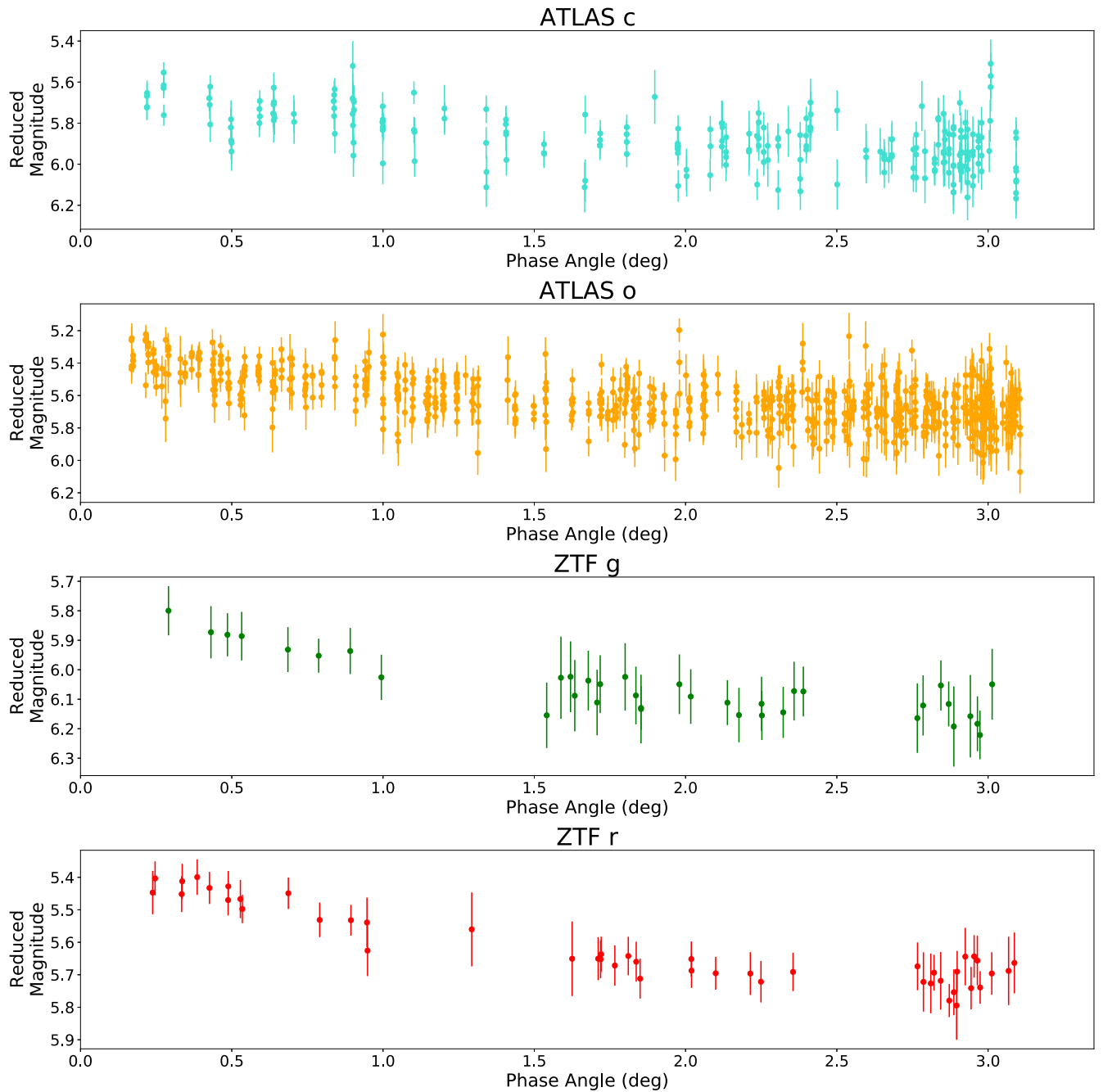
Figure 4. Reduced magnitudes vs. solar phase angle of Chiron from ATLAS and ZTF from the pre-2021 Brightening Event. Error bars are 1σ uncertainties.

magnitude. The color-corrected phase curve of Chiron before, during, and after the 2021 Brightening Event is plotted in Figure 5. These magnitudes were color-corrected to the ATLAS c and o filters using Chiron's pre-Brightening Event $c - g$ and $o - r$ color indices calculated from the absolute magnitude values of linear fits to Chiron's phase curve in each filter. Figures 2 and 3 show the brightness evolution (panels (a) and (c)) and phase curve (panels (b) and (d)) of Chiron in the ATLAS and ZTF data sets, respectively, color-coded by pre-, during, and post-2021 Brightening Event, with the latter two time ranges divided into pre- and postopposition. The ATLAS phase curves of individual post-2021 Brightening Event observing seasons are shown in Figure 6 for clarity. Chiron's phase curves in observing seasons M (2021–2022) and N (2022–2023) are distinct both from each other and compared to

the previous five observing seasons pre-2021 Brightening Event, which all lie on the same profile as shown in Figures 2, 3, 5, and 6 (see Section 4.1.1 for more details). Figure 5 also shows that Chiron's phase curve profile is consistent between different filters across the same observing seasons. Figures 2, 3, and 6 also reveal that Chiron's brightness has evolved significantly within the time span of a single observing season. Postopposition magnitudes in observing season M (2021– 2022) are brighter than those preopposition at the same phase angles. Measuring this difference for the ZTF r filter, we find the postopposition magnitudes to be brighter than preopposition by $\sim 2\sigma$ on average. The ZTF g-filter data postopposition are too sparse to allow an accurate measurement but are consistent with preopposition within the uncertainties. Pre- and postopposition magnitude values in observing season N

9
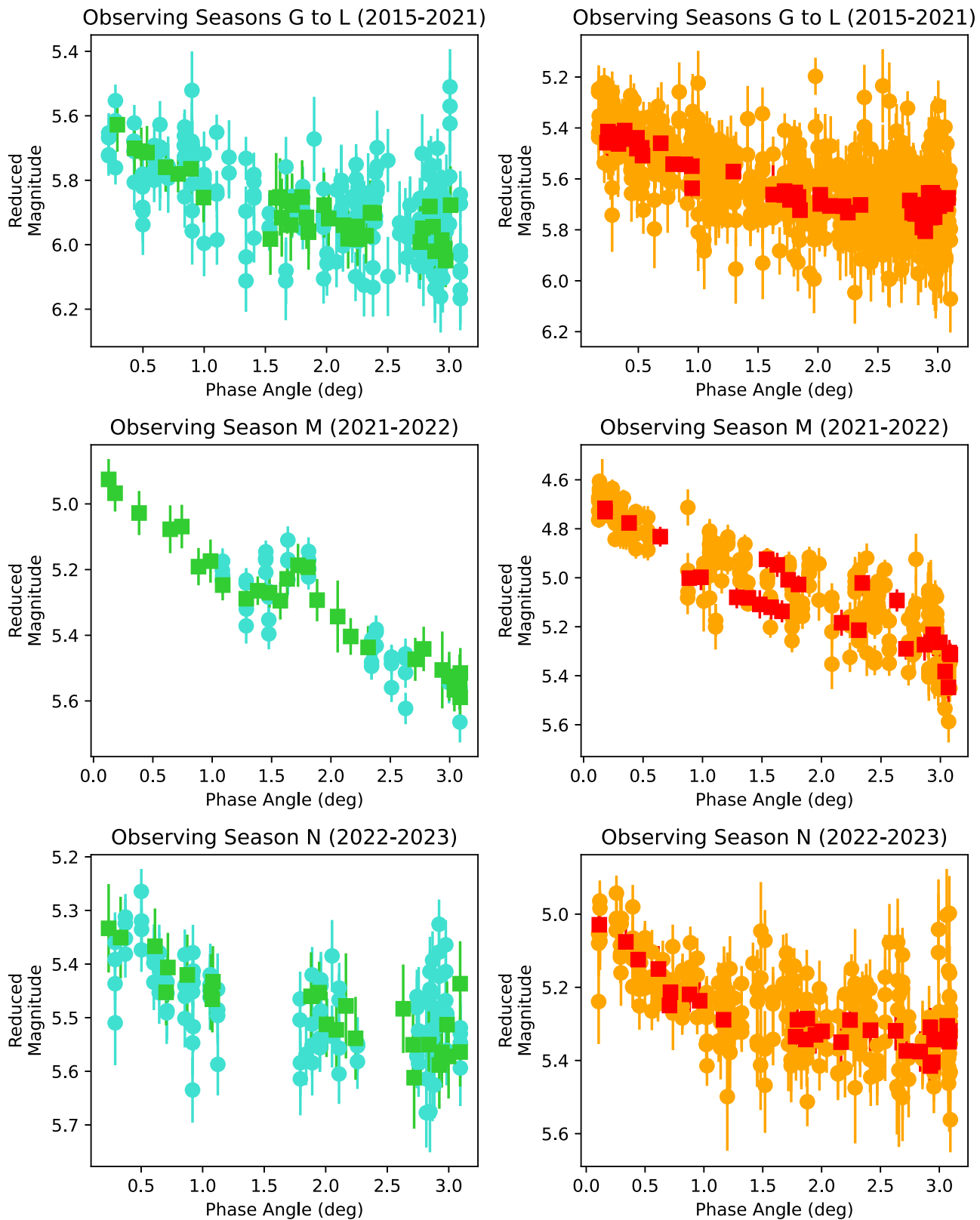
Figure 5. ATLAS *c* (turquoise circles) and ZTF *g* (green squares) color-corrected reduced magnitudes of Chiron vs. solar phase angle (left column) and ATLAS *o* (orange circles) and ZTF *r* (red squares) color-corrected reduced magnitudes of Chiron vs. solar phase angle (right column) for observing seasons G–L (2015–2021; top row), M (2021–2022; middle row), and N (2022–2023; bottom row). Error bars are 1σ uncertainties.

(2022–2023) are also consistent in brightness. Chiron's evolving brightness and phase curve prevents us from fitting its phase curve during the 2021 Brightening Event or after, precluding removal of phase angle effects.

4.1.1. Phase Coefficients

The dense sampling coverage (see Figure 4) of observing seasons I–L before the 2021 Brightening Event by ATLAS
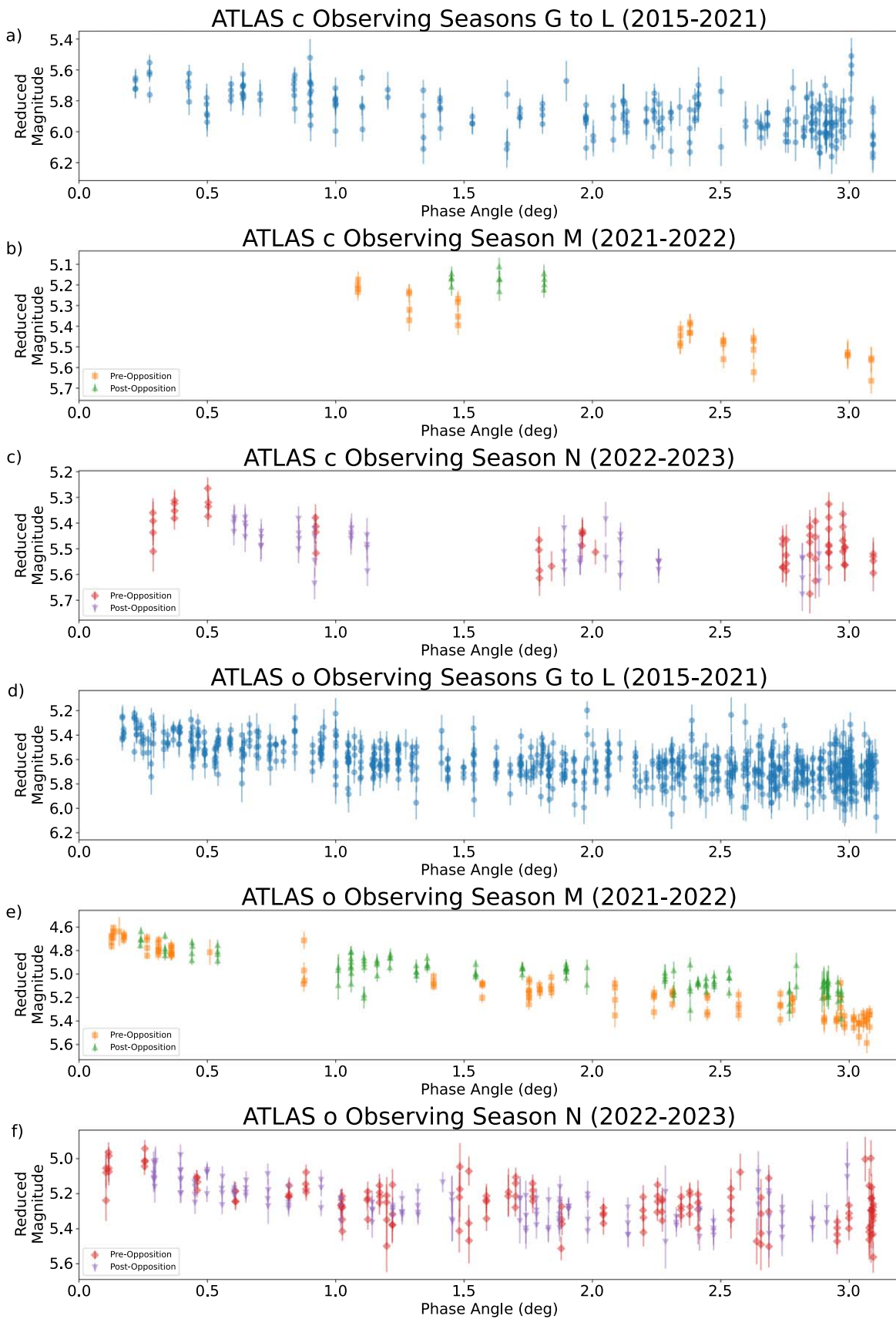
Figure 6. ATLAS phase curves of Chiron across observing seasons in the *c* filter (panels (a), (b), and (c)) and *o* filter (panels (d), (e), and (f)), color-coded the same as Figure 2. Error bars are 1σ uncertainties.

Table 3
ATLAS o-filter Phase Coefficients for Observing Seasons Pre- and Post-2021 Brightening Event

Observing Season	β_o (mag deg^{-1})	N_o
I (2017–2018)	0.105 ± 0.012	235
J (2018–2019)	0.115 ± 0.013	176
K (2019–2020)	0.092 ± 0.012	178
L (2020–2021)	0.093 ± 0.011	178
M (preopposition 2021)	0.226 ± 0.008	108

Note. Uncertainties are 2σ errors.

allows us to measure the linear phase coefficient of Chiron in each observing season utilizing the same methods and criteria of Dobson et al. (2023). We find that Chiron's phase curve has remained relatively unchanged from 2012 up to the 2021 Brightening Event (observing seasons D–L). The o-filter linear phase coefficient values of each observing season I–M are listed in Table 3 and are consistent to 2σ within uncertainties, in accordance with the findings of Betzler (2023). The comparatively sparser sampling of the ATLAS c filter compared to o means we can only accurately measure the linear phase coefficient for observing season L. Comparing the c-filter linear phase coefficient value for observing season L, $\beta_c = 0.110 \pm 0.018$ mag deg^{-1}, to that of the entire ATLAS baseline as measured by Dobson et al. (2023; $\beta_c = 0.093 \pm 0.011$ mag deg^{-1}), we find them to be consistent within uncertainties. Figures 2, 3, and 6 highlight that Chiron's phase curve changed in shape during and post-2021 Brightening Event. This would cause different linear phase coefficient values when measured across preopposition magnitude values compared to postopposition ones and would lead to an inaccurate value when measured across the entire observing season. We therefore select only preopposition data points of observing season M (2021–2022) to reduce the effect of Chiron's evolving phase curve and fit a linear phase curve function to the ATLAS o-filter reduced magnitudes to quantify by how much the phase curve has changed. The preopposition ATLAS c-filter data set for observing season M (2021–2022) is too sparse for an accurate phase curve fit. We find a linear phase coefficient value $\beta_o = 0.226 \pm 0.008$ mag deg^{-1}, differing significantly from the pre-2021 Brightening Event value measured by Dobson et al. (2023; $\beta_o = 0.097 \pm 0.006$). The presence of a dust coma may have caused this change in the phase coefficient of Chiron, but the uncertainties and scatter of our ATLAS and ZTF observations prevent us from constraining the presence of a dust coma before Chiron's 2021 Brightening Event. Furthermore, although a standard phase curve model for cometary comae exists (Schleicher 2010),[23] it may not be applicable to Centaur comae if the mechanism that produces them or the type of dust emitted is different for comets. A detailed analysis of the effect of dust on Chiron's phase curve is therefore beyond the scope of this paper.

4.2. Color Evolution

We use the dual filter coverage of the ATLAS and ZTF data sets to look for any potential changes in Chiron's $c - o$ and $g - r$ colors across time. We cannot correct our reduced magnitudes for

---

[23] https://asteroid.lowell.edu/comet/dustphase/details

phase angle as Chiron's phase curve evolved significantly during observing seasons M (2021–2022, the Brightening Event) and N (2022–2023, post-Brightening Event). Therefore, we utilize two methods to minimize the phase angle effects on our observations. First, for a given data point in one filter, we select the data point in the other filter closest in time, under the criterion that it is separated in time by $\leqslant 2$ days (the approximate observation cadence of ATLAS) in order to identify any sudden changes in Chiron's color index. We use the reduced magnitude value of each observation to calculate Chiron's $c - o$ and $g - r$ color values and associated uncertainties. The second method involves fitting polynomial splines to its reduced magnitude values across time. By interpolating reduced magnitude measurements across time, we may better account for Chiron's evolving brightness and phase curve, including any sudden increase/decrease in magnitude. We generate 10^3 synthetic lightcurves for each filter in a given observing season by offsetting each magnitude value by a random number generated from a Gaussian distribution with standard deviation equal to the magnitude uncertainty. We then fit third-order polynomial splines to each synthetic lightcurve using the *interpolate* package of the *scipy* Python library (Virtanen et al. 2020). For a given data point of a given synthetic lightcurve in one filter, we extrapolate Chiron's brightness at that time in the other filter based on the fitted spline. We then use the resulting reduced magnitude values to calculate a $c - o$ and $g - r$ color value. We only perform this second method for observing seasons with $\geqslant 25$ observations in a given filter, ensuring that the polynomial can fit Chiron's magnitude values accurately.

Figure 7 shows the resulting ATLAS $c - o$ and ZTF $g - r$ color indices of Chiron across time, calculated from temporally adjacent points. The ATLAS $c - o$ and ZTF $g - r$ values as calculated from the spline-fitting method are shown in Figures 8 and 9, respectively. We find that Chiron has not undergone any significant color evolution across the baselines of ATLAS and ZTF, as Figures 7, 8, and 9 show that Chiron's color has remained constant within uncertainties across this time.

Simultaneous g- and r-band measurements of Chiron were also obtained from our Gemini observations at three epochs (see Table A8). The sparse number of data points from Gemini combined with the evolution of Chiron's phase curve means we can only compare the Gemini $g - r$ values within a season. The two data points from season K are separated in phase angle by $\lesssim 0.\!^{\circ}2$, allowing comparison, as the brightness variation due to phase angle will be minimal. The distance-corrected $g - r$ values of the two data points of observing season N (2022–2023), $g - r = 0.501 \pm 0.057$ and $g - r = 0.557 \pm 0.052$, and are consistent to 1.0σ.

4.3. Search for a Coma and PSF Extension

Beyond photometry, we also analyze our Gemini and TRAPPIST-South observations for a visible coma and PSF extension. Chiron has previously exhibited a visible coma during instances of brightening (Hartmann et al. 1990; Silva & Cellone 2001; Duffard et al. 2002). However, Dobson et al. (2021) found no visible coma or PSF extension in ATLAS and LOOK observations during Chiron's 2021 Brightening Event. We stack our Gemini observations to search for any faint coma or PSF extension exhibited by Chiron during or post-2021 Brightening Event. The stacked images at the coordinates of Chiron from each of the five epochs listed in Table A8 are shown in Figure 10 in the r and i filters. Our filter choice is
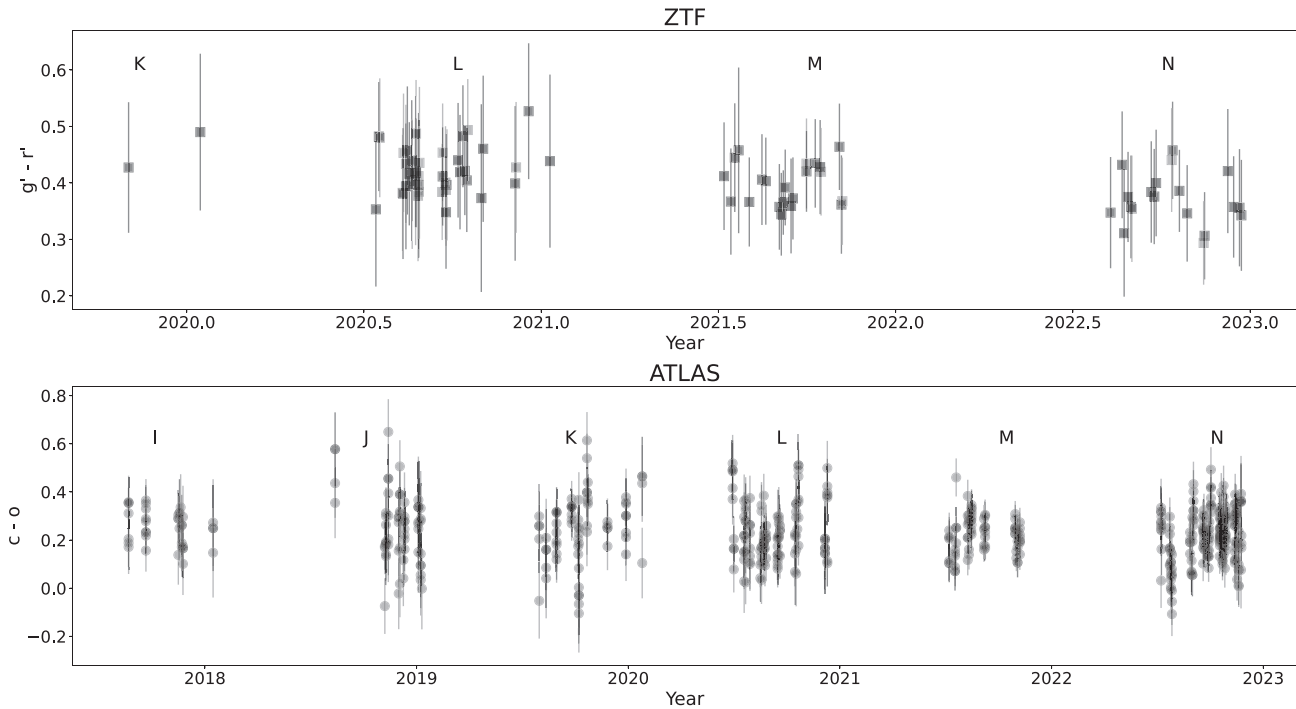
Figure 7. ZTF (upper) and ATLAS (lower) color index values calculated from temporally adjacent data (⩽2 days apart) plotted across time. All observing seasons are labeled as per Table 2. Error bars are 1σ uncertainties.

motivated by the physical reality that the *r* and *i* filters are free from the brightest gas emission features in comets (Figure 1 in Feldman et al. 2004); the only detection of optical gas emission at Chiron previously reported was the CN (0–0) band at 3883 Å by Bus et al. (1991) during its active phase in 1990. No comae or tails are visible in any of the stacked Gemini images. We search for PSF extension by measuring the radial profiles of Chiron's PSF in each stacked image and comparing the result with field stars. We utilize SExtractor Python (Bertin & Arnouts 1996; Barbary 2016) to detect background sources in our observations. We select field stars for comparison to Chiron on the basis that (1) the peak flux count of their PSF does not exceed 50,000 electrons, to ensure they are not saturated; (2) they are distant from neighboring stars by at least the outer radius of any applied circular annulus for photometry; (3) they are brighter than 22nd magnitude, to ensure they are clearly visible in our images; (4) the uncertainties of both their catalog magnitude and the difference between their instrumental magnitudes and their Pan-STARRS1 catalog magnitudes are both less than 0.075 mag; (5) their catalog $g - r$ colors are within the range $-0.5 \leqslant g - r \leqslant 2.0$; (6) the difference between their catalog PSF magnitudes and Kron magnitudes in the *i* filter is less than 0.05 mag so that we can separate stars from galaxies; and (7) their residuals to an unweighted linear fit to their difference in instrumental and catalog magnitudes as a function of catalog color index $g - i$ are less than 2.5σ. We utilize the *RadialProfile* function from the *photutils* Python library (Bradley 2023) to measure the radial profiles of Chiron and the background field stars. We apply a circular aperture of radius 13 pixels to both Chiron and the background field stars. To remove the flux contribution from the background, we utilize a background annulus aperture of inner and outer radii of 21.4 and 35.7 pixels, respectively, calculating the total background value from the product of the annulus area and

the 3σ-clipped median background value from the annulus. We subtract this total background flux value from the corresponding radial profile. An example of the resulting radial profiles is shown in Figure 11, where no visible coma is detected. Chiron's PSF is consistent with those of the background stars in all filters for all five epochs of observation.

We also searched for signs of activity in our TRAPPIST-South observations (pre-Brightening Event, spanning 2012–2015), whose relatively large data sets and time span allow a probe into past cometary behavior. Neither visible comae nor tails are visible in any of our TRAPPIST-South observations. We searched for PSF extension by comparing the PSF profiles of Chiron to those of the field stars using the same method as Devogèle et al. (2021). We created two stacks for each night, a first one on Chiron, compensating for its proper motion, and a second one on the background field stars. We then computed the distances of each pixel from the centroids of the PSFs of Chiron and the background stars, respectively. The radial profiles of Chiron were found to be identical to the field stars for every epoch.

4.4. Rings

To ascertain if Chiron's reported ring system together with a changing viewing angle as seen from Earth could explain the Centaur's observed brightness evolution, we reconstruct the ring model as constructed by Ortiz et al. (2015). We include flux contributions from Chiron's nucleus, its two rings as reported by Ortiz et al. (2015) based on observations of Chiron's 2011 occultation, and the 1970 cometary outburst, utilizing a ring albedo[24] value of $p_V = 0.18$ and ring widths of 6.6 and 4.7 km (private communication with [anonymized for

---

[24] Ortiz et al. (2015) quote the albedo value of Chiron's rings as $p_V = 0.17$; however, we can only reproduce their model using an albedo value of $p_V = 0.18$.

Figure 8. Upper plot: ATLAS *c*-filter reduced magnitudes (turquoise circles) vs. time with third-order interpolated splines fitted to synthetic data overplotted (red). Center plot: ATLAS *o*-filter reduced magnitudes (orange circles) vs. time with third-order interpolated splines fitted to synthetic data overplotted (teal). Lower plot: color index value calculated from the predicted magnitudes in each filter from the synthetic splines plotted across time. Red circles denote nominal color index values with green lines highlighting the range that includes the central 68.3% of synthetic values, therefore corresponding to 1σ uncertainties. All observing seasons are labeled as per Table 2.

dual-anonymous review]). We calculate the aspect angle δ of Chiron at a given time and corresponding ecliptic coordinates according to the equation

$$\delta = \frac{\pi}{2} - \arcsin[\sin(\beta_e)\sin(\beta_p) + \cos(\beta_e)\cos(\beta_p)\cos(\lambda_e - \lambda_p)], \quad (1)$$

where β_e and λ_e are the ecliptic latitude and longitude, respectively, of Chiron as observed from Earth and β_p and λ_p are the ecliptic latitude and longitude of the pole orientation of Chiron and its ring system. We then calculate the projected area $A_p(\delta)$ of Chiron at a given epoch and corresponding aspect angle δ according to the equation

$$A_p(\delta) = \frac{\text{Area}_{\max}(\delta) + \text{Area}_{\min}(\delta)}{2}, \quad (2)$$

where $\text{Area}_{\max}(\delta)$ and $\text{Area}_{\min}(\delta)$ are the maximum and minimum projected area defined by the following equations:

$$\text{Area}_{\max}(\delta) = \pi a[b^2\cos^2(\delta) + c^2\sin^2(\delta)]^{1/2} \quad (3)$$

and

$$\text{Area}_{\min}(\delta) = \pi b[a^2\cos^2(\delta) + c^2\sin^2(\delta)]^{1/2}, \quad (4)$$

where a, b, and c are the semimajor axes of Chiron's nucleus assuming a triaxial ellipsoid shape in hydrostatic equilibrium. We use the same equation as Ortiz et al. (2015) to calculate the ratio of Chiron's total computed flux F_{Chiron} to that of the Sun F_{Sun} at a given time t and corresponding aspect angle α, given by

$$\frac{F_{\text{Chiron}}}{F_{\text{Sun}}} = A_p p_V f(\alpha) + p_V^{\text{Ring1}} f'(\alpha)\pi((a_1 + W_1)^2 - a_1^2)\mu$$
$$+ p_V^{\text{Ring2}} f'(\alpha)\pi((a_2 + W_2)^2 - a_2^2)\mu + A_c p_d \exp(-(t - t_0)/\tau_d), \quad (5)$$

where A_p is the projected area of Chiron's nucleus; p_V is the geometric albedo of the nucleus; $f(\alpha)$ is the solar phase function of the nucleus (taken to equal 1); p_V^{Ring1} and p_V^{Ring2} are the geometric albedos of the first and second rings, respectively; $f'(\alpha)$ is the solar phase function of the rings (taken to
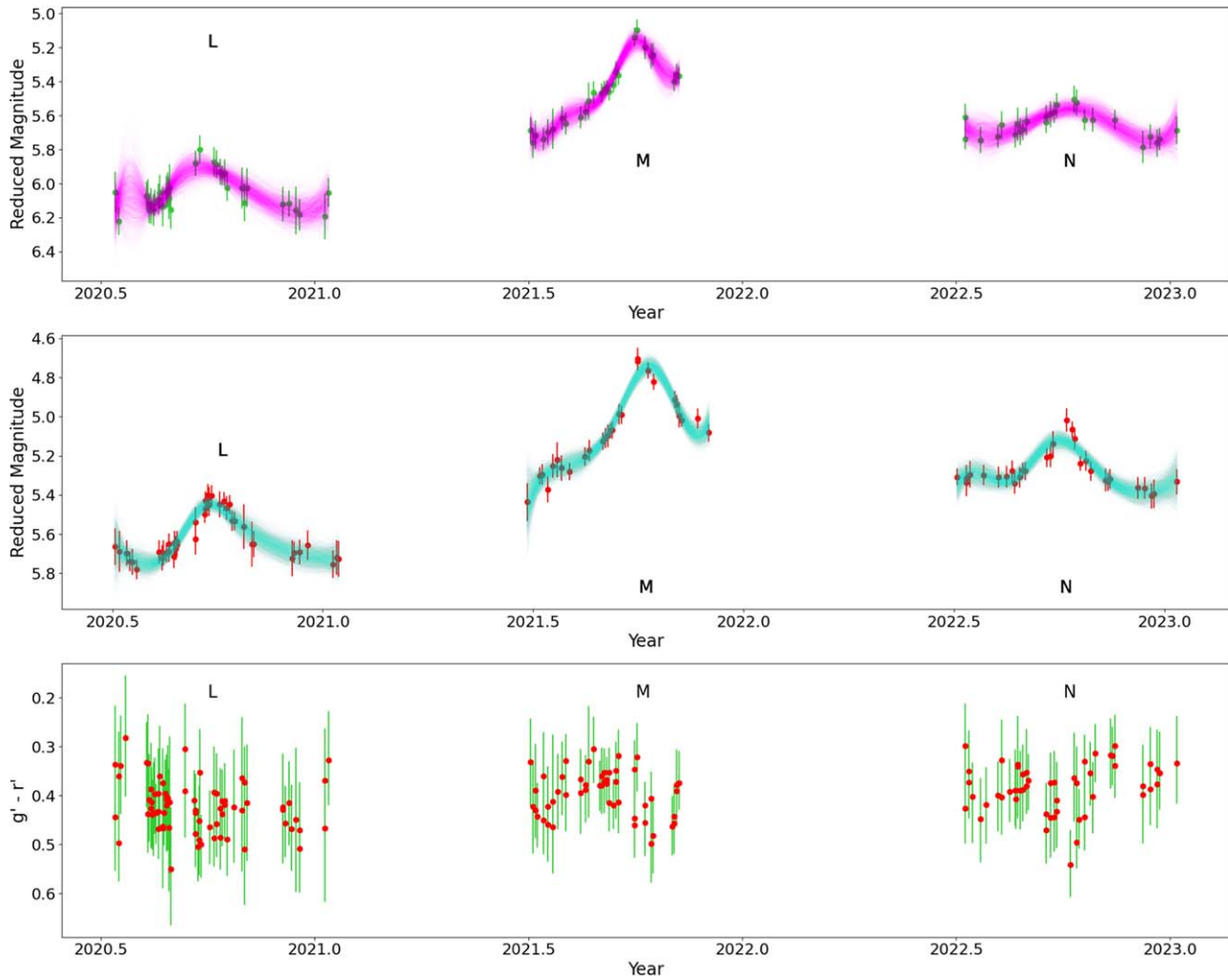
Figure 9. Upper plot: ZTF g' -filter reduced magnitudes (green circles) vs. time with interpolated third-order splines fitted to synthetic data overplotted (magenta). Center plot: ZTF r'-filter reduced magnitudes (red circles) vs. time with interpolated third-order splines fitted to synthetic data overplotted (turquoise). Lower plot: color index value calculated from the predicted magnitudes in each filter from the synthetic splines plotted across time. Red circles denote nominal color index values with green lines highlighting the range that includes the central 68.3% of synthetic values, therefore corresponding to 1σ uncertainties. All observing seasons are labeled as per Table 2.

equal 1); μ is the absolute value of the cosine of the rings' aspect angle; $\pi((a_i + W_i)^2 - a_i^2)$ is the projected area of the i ring, where W_i is the width of the i ring and a_i is the radial distance of each ring to Chiron's nucleus; A_c is the initial scattering cross section of the coma caused by Chiron's 1970 cometary outburst; t_0 is the initial time at which the coma dust cloud starts to decay; and τ_d is the decay time of the coma. We utilize the same parameter values of Ortiz et al. (2015) for the cometary outburst contribution. We then compute Chiron's resulting absolute magnitude H_V across time using the following equation:

$$H_V = H_{V,\text{Solar}} + 2.5 \log_{10}\left(\pi \frac{(1.496 \times 10^8)^2}{(F_{\text{Chiron}}/F_{\text{Sun}})} \right), \quad (6)$$

where $H_{V,\text{Solar}}$ is the absolute magnitude of the Sun, which we take to equal -26.76 (Willmer 2018).

We also collate all absolute magnitude measurements of Chiron from the literature (Bus et al. 2001; Silva & Cellone 2001; Duffard et al. 2002; Bauer et al. 2003; Romon-Martin et al. 2003; Groussin et al. 2004; Bagnulo

et al. 2006; Belskaya et al. 2010; Fornasier et al. 2013; Galiazzo et al. 2016; Cikota et al. 2018), applying a consistent phase angle correction to all values utilizing the HG phase curve model with slope parameter $G = 0.70$ as determined by Bus et al. (2001). We transform the magnitude measurements from our own observations to the Johnson–Cousins V filter. For a given filter, we calculate the mean reduced magnitude of any observations taken before the 2021 Brightening Event. We then calculate the mean reduced magnitude of any V-filter observations (our own or from the literature) that coincide in time. The difference between these means is subtracted from every observation in the given filter. No V-filter measurements exist post-2021 Brightening Event, so we use the filter-corrected ATLAS o observations, divided by pre- and postopposition in each observing season, to transform the Gemini and LOOK magnitudes. We transform our filter-corrected reduced magnitudes to absolute magnitudes H_V by applying a phase angle correction using $G = 0.70$ as per Bus et al. (2001). All the collated absolute magnitude values of Chiron, both from this work and from previous literature studies, are listed in Table 4.

Figure 12 shows the estimated absolute magnitude of Chiron over time combining our data sets and measurements from the
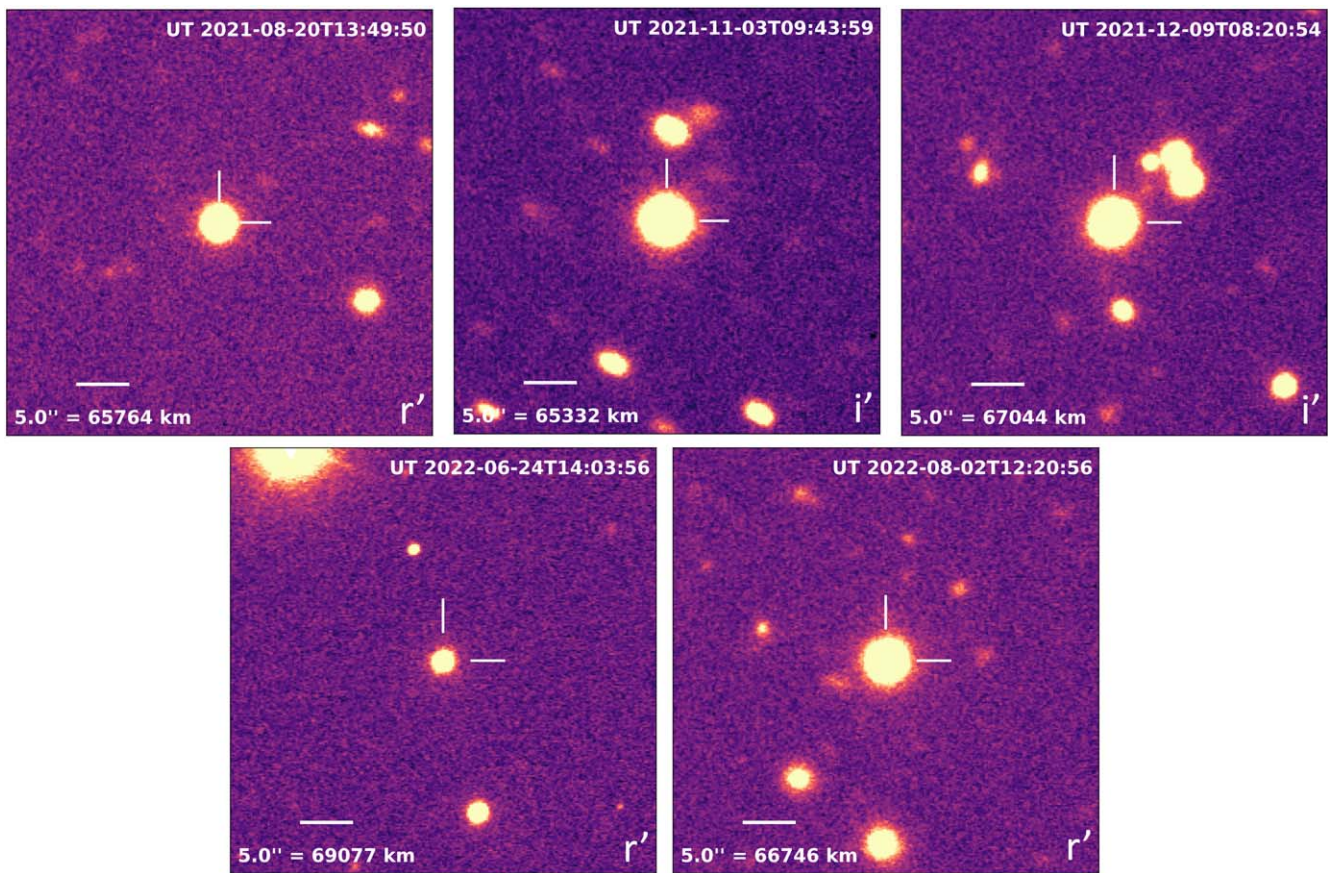
Figure 10. Gemini stacked observations of Chiron in the r' and i' filters at all five epochs of observation. Crosshairs indicate Chiron's position in each of the images. No comae or tails are visible in any of the images. The varying size of Chiron in each image is due to seeing variations and also relative image scales between individual nights. Note: equatorial north is up and east to the left.
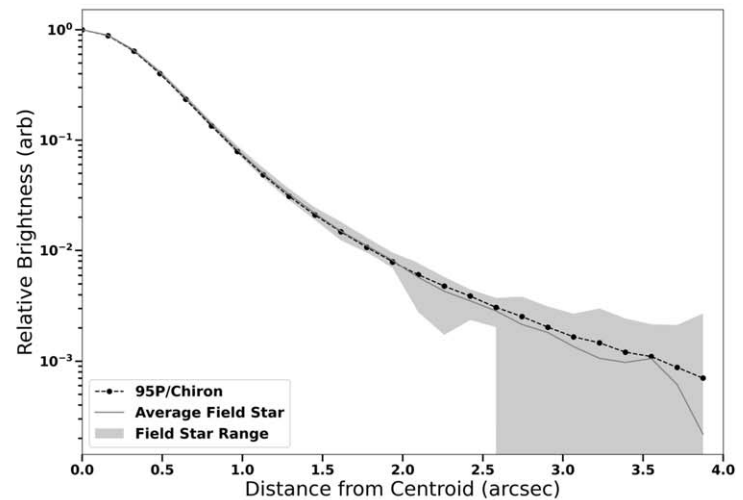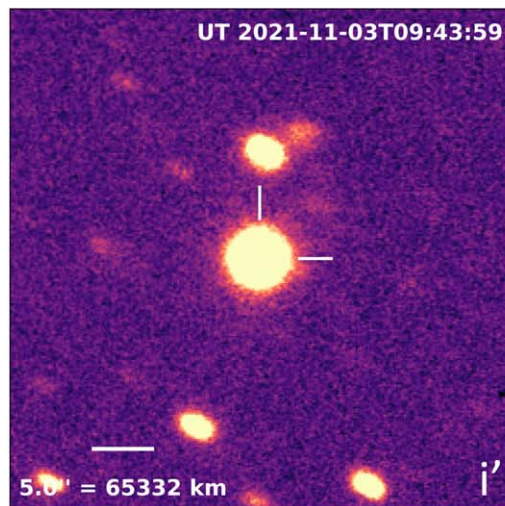
Figure 11. Gemini stacked observation of Chiron in the i' filter for 2021 November 3 with corresponding PSF radial profiles of Chiron and background field stars. Crosshairs indicate Chiron's position in the image. The PSF profile of Chiron is consistent with those of background stars.

literature as compared to Ortiz et al. (2015). Chiron's absolute magnitude across our baseline of observations is shown in Figure 13 for clarity. As seen in Figures 12 and 13, the latter showing the post-Brightening Event era, Chiron's brightness evolution across our baseline of observations is inconsistent with that predicted by Ortiz et al. (2015). The high-precision Pan-STARRS, DES, ZTF, and Gaia measurements show that even before 2021, Chiron was already significantly brighter

than predicted by Ortiz et al. (2015). The ring model predicted that Chiron would slowly dim across observing seasons M (2021–2022, the 2021 Brightening Event) and N (2022–2023, post-Brightening Event). However, Chiron's measured absolute magnitude from ATLAS, ZTF, LOOK, and Gemini was significantly brighter than the Ortiz et al. (2015) ring model during this time, differing by ∼0.5–1 mag and reaching a peak magnitude comparable to its historical maximum brightness in

Table 4
Estimated Absolute Magnitudes of Chiron

UT Year	Geocentric Distance	Heliocentric Distance	Phase Angle	Apparent Magnitude	Apparent Magnitude Uncertainty	Reduced Magnitude	Filter	Estimated Absolute Magnitude	Estimated Absolute Magnitude Uncertainty	Reference
	(au)	(au)	(deg)							
2023.098537	19.343	18.807	2.485	18.111	0.055	5.3068	r'	5.2661	0.055	This work
2023.098531	19.343	18.807	2.485	18.475	0.079	5.6708	g'	5.2734	0.079	This work
2023.098524	19.343	18.807	2.486	18.127	0.056	5.3228	r'	5.2821	0.056	This work
2023.098518	19.343	18.807	2.486	18.485	0.078	5.6808	g'	5.2834	0.078	This work
2023.093077	19.314	18.807	2.540	18.125	0.063	5.3240	r'	5.2812	0.063	This work
2023.093071	19.314	18.807	2.540	18.453	0.074	5.6520	g'	5.2526	0.074	This work
2023.093064	19.314	18.807	2.540	18.164	0.060	5.3630	r'	5.3202	0.060	This work
2023.093058	19.314	18.807	2.541	18.556	0.078	5.7550	g'	5.3556	0.078	This work
2023.076629	19.225	18.809	2.689	18.071	0.082	5.2799	r'	5.2319	0.082	This work
2023.076623	19.225	18.809	2.689	18.611	0.093	5.8199	g'	5.4152	0.093	This work

Note. The paper Bus et al. (2001) does not provide values for apparent magnitude, its associated uncertainty, or reduced magnitude.

(This table is available in its entirety in machine-readable form in the online article.)

the 1970s (Bus et al. 2001). The Ortiz et al. (2015) ring model fails to match Chiron's brightness evolution across our baseline of observations and therefore cannot explain the 2021 Brightening Event.

5. Discussion

Chiron's observed increase in brightness from 2021 onward far exceeds its amplitude of rotational modulation, predicted to be ≲0.05 mag during 2021 (Ortiz et al. 2015) when phase-folded to its measured rotation period of 5.917813 hr (Bus et al. 1989; Marcialis & Buratti 1993), and was too small to be measured in ATLAS data from Dobson et al. (2021). Furthermore, Chiron's observed increase in brightness exceeds its brightness variation due to its phase function. We therefore rule out both Chiron's rotation and phase curve as being responsible for the 2021 Brightening Event. Betzler (2023) hypothesized that Chiron's observed evolution in brightness could instead be due to variation in surface albedo, with areas of differing albedo becoming visible to Earth as the Centaur's aspect angle changes throughout its orbit. However, comparing pre- and postopposition ATLAS and ZTF observations from observing season M (2021–2022), we have seen that Chiron's brightness evolved significantly, at an appreciable rate across the time span of a single observing season. The short timescale of Chiron's observing season M (0.6 yr) compared to its orbit around the Sun (50.8 yr) means that Chiron has only swept through 1.2% of its orbit during this time. Combined with the measured ecliptic coordinates of Chiron's axial pole of $\lambda = 151° \pm 8°$ and $\beta = 18° \pm 11°$ (Ortiz et al. 2023) implying a near face-on obliquity to Earth, as well as the Centaur's small amplitude of rotational modulation, we consider it implausible for a surface feature on Chiron as suggested by Betzler (2023) to enter and exit the view from Earth across such a small percentage of the object's orbit. We thus reject surface albedo variations as being responsible for Chiron's brightening and dimming across 2021–2023.

We also consider the Chiron ring system model proposed by Ortiz et al. (2015) to be an unlikely cause of the object's observed brightening during and since 2021. Reconstructing this model, we find Chiron's measured absolute magnitudes to be significantly brighter than predicted by ∼0.5–1 mag.

Furthermore, the timescale on which Chiron's 2021 Brightening Event occurred is too short to be explained by the ring model, which predicts variation in Chiron's absolute magnitude across decadal time spans. The Ortiz et al. (2015) lightcurve also fails to replicate the long-term evolution of Chiron's absolute magnitude both pre- and post-2021 Brightening Event. Chiron was predicted to slowly dim over time when it instead was observed to brighten in 2021. Additionally, Chiron was also significantly brighter pre-2021 Brightening Event than predicted by the ring model. We note, however, that although the Ortiz et al. (2015) model cannot explain either the 2021 Brightening Event or Chiron's brightness evolution before this across our observation baseline, this does not completely rule out the possibility that Chiron's rings are not well described by current models and are at least partially responsible for this brightening in reduced magnitude. Analyses of stellar occultations by Chiron in 2018 and 2022 indicate evolution of the material surrounding Chiron on relatively short timescales (Braga-Ribas et al. 2023; Ortiz et al. 2023; Sickafoose et al. 2023). Sickafoose et al. (2023) found Chiron's rings, as measured during the 2018 occultation, to be of reduced optical depth compared to 2011, with a reported feature, potentially indicative of a third ring, detected during immersion but not during emersion. Furthermore, Ortiz et al. (2023) detected signals indicative of additional, previously undiscovered ring-like features during Chiron's 2022 occultation with the signals of the already-known rings being more pronounced compared to 2011, indicating a significant change in the ring system's configuration. Occultation studies also reveal that Chiron's rings are not azimuthally homogeneous in width (Ortiz et al. 2023), exhibiting agglomerations of ring particles possibly caused by small, unseen shepherd satellites. Collisions of satellites have been proposed as one mechanism for creating Centaur rings (Braga-Ribas et al. 2014; Ortiz et al. 2015; Melita et al. 2017), and such an event could act to augment Chiron's ring system and thus its apparent brightness as seen from Earth. Future occultation studies are necessary to reveal the true nature of the reported ring system surrounding Chiron in order to better estimate its contribution to the Centaur's changing brightness across time.
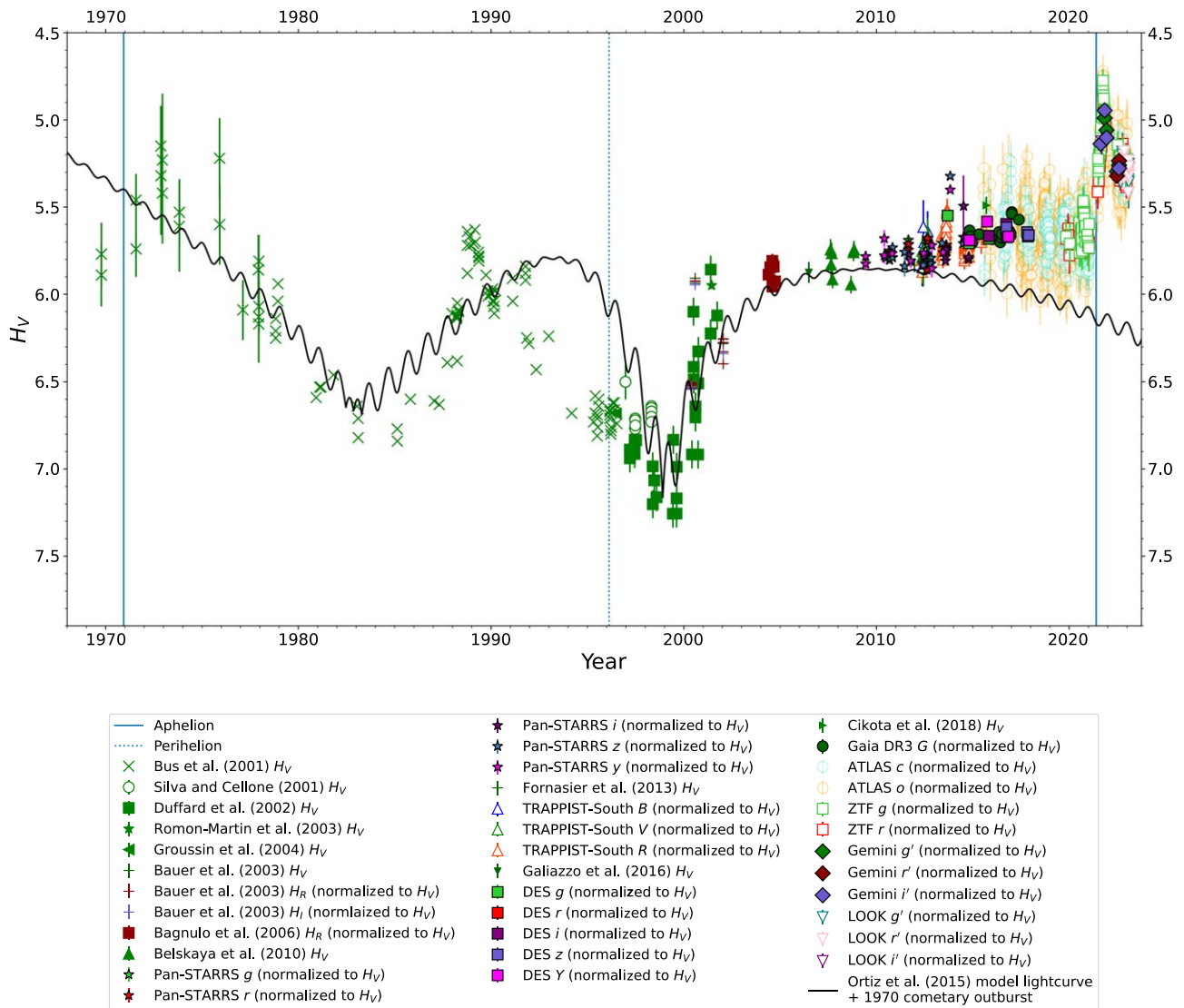
Figure 12. Estimated *V*-band absolute magnitude (corrected for distance, phase angle, and filter color difference) vs. time of Chiron, with values obtained from our observations and literature measurements. Dates of aphelion and perihelion are indicated by the blue vertical solid and dotted lines, respectively. Chiron was known to exhibit a visible coma during its outburst commencing around 1989 (Meech & Belton 1989; Hartmann et al. 1990; Meech 1990), with later confirmed detections of a coma in 1998 (Silva & Cellone 2001). Chiron was observed to dim in brightness as it approached perihelion in 1996 February, reaching its dimmest recorded absolute magnitude shortly after perihelion around 1999. Other likely cometary outbursts are thought to have occurred in the 1970s (Bus et al. 2001) and around the year 2000 (Duffard et al. 2002) as evidenced by Chiron's sudden increases in absolute magnitude around these times. The lightcurve as predicted from the ring model of Ortiz et al. (2015) is plotted in black. Chiron's 2021 Brightening Event contrasts with the gradual dimming as predicted by Ortiz et al. (2015).

Despite the need for an improved understanding of Chiron's rings, we argue that Chiron's observed evolution in brightness from 2021 onward is better described by an epoch of cometary activity. The increase in brightness in 2021 followed by a dimming across time is consistent with Chiron's observed brightness evolution during previous cometary episodes (e.g., Bus et al. 1989; Meech & Belton 1989). This years-spanning change in brightness, though far longer than the weeks- (Trigo-Rodríguez et al. 2008; Miles 2016; Schambeau et al. 2017, 2019; Peixinho et al. 2020) or months-long (Choi et al. 2006a, 2006b; Jaeger et al. 2011; Rousselot et al. 2016; James 2018; Kareta et al. 2019; Seccull et al. 2019) cometary outbursts of the active Centaurs 29P/Schwassman–Wachmann 1 and 174P/Echeclus, respectively, is nevertheless in keeping with the duration of previous epochs of Chiron's cometary activity, which have also lasted for years (Tholen et al. 1988; Bus et al. 1989; Meech & Belton 1989; Dahlgren et al. 1990;

Hartmann et al. 1990; Luu & Jewitt 1990; Meech & Belton 1990; Meech 1990; West 1990; Bus et al. 2001; Silva & Cellone 2001). Additionally, Ortiz et al. (2023) theorized that material ejected due to an increase in cometary activity in 2021 could augment Chiron's rings, thereby explaining the apparent change in configuration in Chiron's ring system between occultations. Whether such a cometary outburst would represent an increase from quiescence or an entirely new epoch of cometary activity from a previously quiescent state is unclear. We did not detect any visible indicators of activity in the TRAPPIST-South observations spanning the years 2012–2015, yet Cikota et al. (2018) detected a tentative $\sim5''$ length tail-like feature of surface brightness 25.3 mag arcsec^{-2} in their 2015 observations of Chiron. Cikota et al. (2018) also reported that Chiron exhibited fluctuations in brightness exceeding that of background field stars, implying low-level "microactivity." Therefore, we consider the most likely cause
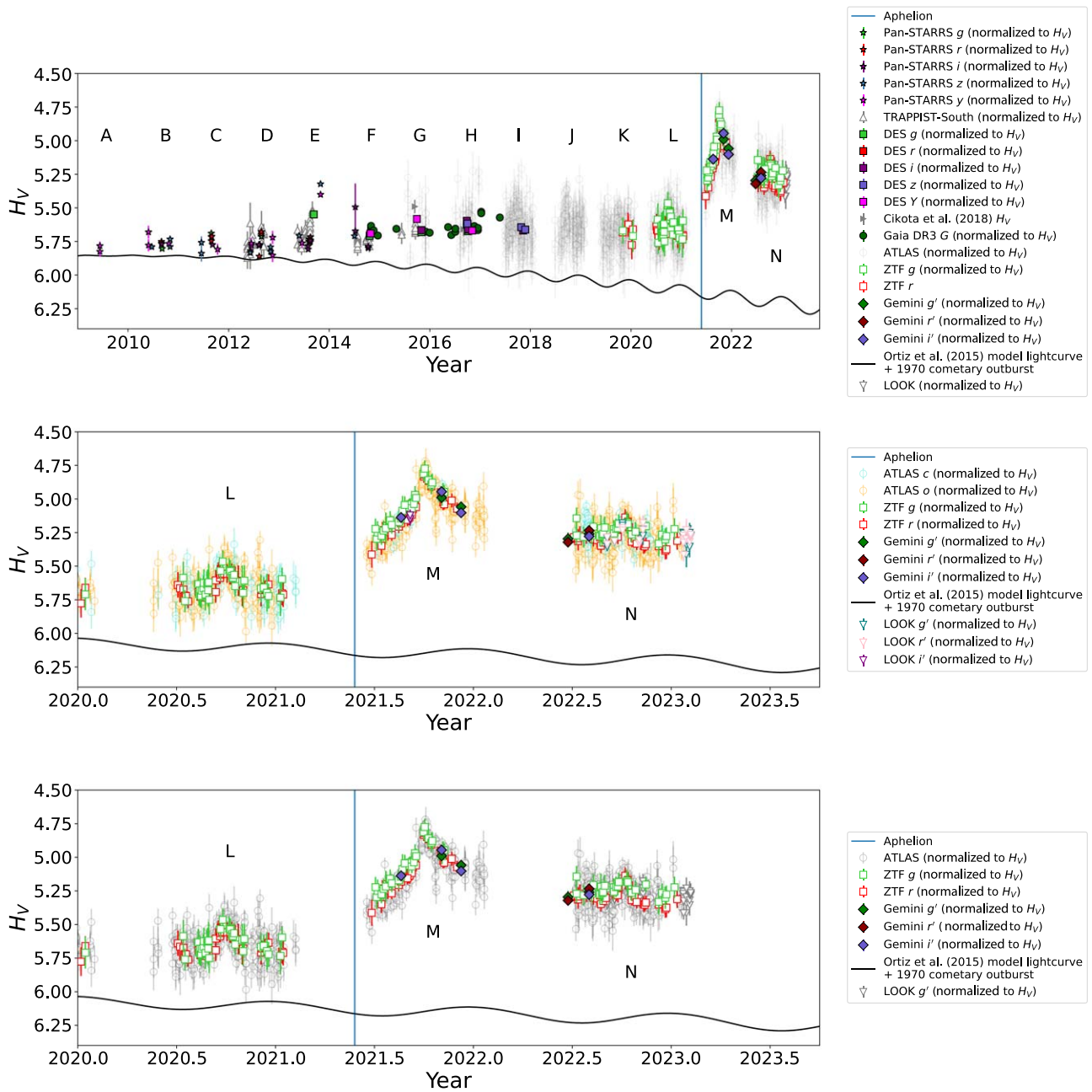
Figure 13. Upper plot: estimated *V*-band absolute magnitude (corrected for distance, phase angle, and filter color difference) vs. time for Chiron across our baseline of observations, with the high-precision observations from Gemini, Gaia, DES, and ZTF highlighted for clarity. Centre plot: estimated *V*-band absolute magnitude (corrected for distance, phase angle, and filter color difference) vs. time for Chiron across observing seasons L–N (2020–2023) highlighting the brightening in Chiron's magnitude due to the 2021 Brightening Event. Lower plot: estimated *V*-band absolute magnitude (corrected for distance, phase angle, and filter color difference) vs. time for Chiron across observing seasons L–N (2020–2023) highlighting the brightening in Chiron's magnitude due to the 2021 Brightening Event. The observations from Gemini and ZTF are highlighted for clarity. All observing seasons are labeled as per Table 2. In all subplots, the date of aphelion is indicated by the solid blue line. Chiron's absolute magnitude as predicted by Ortiz et al. (2015) is plotted in black.

of Chiron's 2021 Brightening Event to be an epoch of either new or increased cometary activity.

If Chiron is presently undergoing cometary activity, an explanation for why we do not detect any visible coma could be that it is too faint to be directly observed beyond the central point spread at Chiron's present heliocentric distance. Previous measurements of Chiron's coma report *V*-band surface brightness values of 24.6 mag arcsec^{-2} (West 1990) in 1990, when Chiron was 11.2 au from the Sun, and 26.0 mag arcsec^{-2} (Silva & Cellone 2001) in 1998 at a heliocentric distance of 8.938 au.

We calculate the limiting magnitudes of our Gemini deep-stacked observations. We utilize the same method of measuring the radial profiles of Chiron and the field stars as Section 4.3 and calculate the limiting surface brightness of each observation at a radial distance from the centroid of Chiron's PSF of 3 times the FWHM of a Gaussian fit to the PSF. We recalculate Chiron's literature coma surface brightness values to the corresponding heliocentric and geocentric distances for each Gemini observation. We transform the limiting surface brightnesses and Chiron's literature coma surface brightnesses

Table 5
3σ Limiting Magnitudes of the Gemini Observations as Compared to the Predicted Brightness of Chiron's Coma

Epoch and Filter	Radial Distance (arcsec)	3σ Limiting Surface Brightness (mag arcsec^{-2})	3σ Limiting Magnitude (mag)	Coma Surface Brightness (W90) (mag arcsec^{-2})	Coma Magnitude (W90) (mag)	Coma Surface Brightness (SC01) (mag arcsec^{-2})	Coma Magnitude (SC01) (mag)
2021-08-20 g	2.8162	22.453	18.209	25.706	20.831	27.796	21.317
2021-08-20 r	2.6550	24.449	20.334	25.686	20.810	27.775	21.297
2021-08-20 i	2.5649	22.650	18.609	25.371	20.496	27.461	20.982
2021-11-03 g	3.6173	24.840	20.053	25.704	20.814	27.794	21.301
2021-11-03 i	2.8325	23.815	19.559	25.371	20.481	27.461	20.968
2021-12-09 g	3.7897	23.756	18.867	25.714	20.880	27.804	21.367
2021-12-09 i	3.2656	23.859	19.294	25.371	20.537	27.461	21.024
2022-06-24 g	1.6347	24.037	20.975	25.684	20.915	27.774	21.402
2022-06-24 r	1.4345	23.442	20.663	25.681	20.912	27.771	21.399
2022-08-02 g	2.9405	24.923	20.586	25.683	20.840	27.773	21.327
2022-08-02 r	2.6914	24.373	20.228	25.681	20.837	27.770	21.324
2022-08-02 i	2.4350	23.670	19.742	25.367	20.524	27.457	21.011

Note. Coma brightness values have been converted to the corresponding filter of each Gemini observation. W90: West (1990); SC01: Silva & Cellone (2001).

M_{surface} into total magnitudes M according to the equation

$$M = M_{\mathrm{surface}} - 2.5\log_{10}(2\pi r^2), \tag{7}$$

where r is the radial distance of the surface brightness measurement from the PSF centroid (Lowry & Fitzsimmons 2005). We then transform Chiron's coma values to the corresponding Pan-STARRS filter of each Gemini observation, transforming first from Johnson–Cousins to SDSS photometric systems and then from SDSS to Pan-STARRS. To transform from Johnson–Cousins to SDSS, we utilize the transformation equations of Jester et al. (2005) for stars with Johnson–Cousins color indices $R_c - I_c < 1.15$ and $U - B \geqslant 0$. These require $B - V$ and $R_c - I_c$ color index measurements of Chiron's coma; we use the $B - V = 0.3$ measurement from West (1991) for this transformation, and in the absence of a historical $R_c - I_c$ measurement of Chiron's coma, we utilize the color index value $R - I = 0.36$ (Galiazzo et al. 2016) of Chiron itself as a proxy. We then use the transformation equations of Finkbeiner et al. (2016) to transform these SDSS values into the Pan-STARRS photometric filter system. We utilize Chiron's $g - i$ color as measured in each epoch of Gemini observations; if an epoch lacks such a measurement, we instead use the closest $g - i$ measurement in time to that epoch. Table 5 shows our resulting 3σ limiting magnitudes for each observation with Chiron's corresponding predicted coma brightness. For all our Gemini observations, for both surface brightness and total magnitude, we find Chiron's coma brightness to be fainter than the 3σ limiting magnitude of the observation, assuming a similar coma to that observed in 1990.

Alternatively, the lack of a detected coma could be due to the mass of the Centaur's nucleus. The large size of Chiron (volume-equivalent radius ∼98 km; Braga-Ribas et al. 2023) compared to most cometary nuclei means its gravitational force is nonnegligible. Some material emitted during an active epoch may be bound to the nucleus if its escape velocity exceeds the grain velocities of the emitted particles, preventing the formation of a spatially extended coma detectable from Earth-based observations. A bound coma around Chiron was previously discovered in 1993 by Meech et al. (1997) using the Hubble Space Telescope. These revealed that Chiron's

brightness profile could only be explained by a coma whose structure comprised two components, one spatially extended and the other bound to the nucleus within its exopause (Meech et al. 1997). To ascertain the possibility that an entirely bound coma could exist around Chiron, we estimate its nuclear escape velocity via the equation

$$v_{\mathrm{esc}} = \sqrt{\frac{4\pi G\rho abc}{3r}}, \tag{8}$$

where G is the gravitational constant; ρ is the density of Chiron's nucleus; a, b, and c are the semimajor axes of the nucleus assuming the triaxial ellipsoidal shape of Braga-Ribas et al. (2023); and r is the equivalent volume radius of the nucleus. Braga-Ribas et al. (2023) estimated Chiron's density to be 1.119 g cm^{-3} based on a Jacobi ellipsoidal model of its shape derived from stellar occultations under the assumption of hydrostatic equilibrium. As this value is model-dependent, we also estimate a range of escape velocity values for Chiron by utilizing the density estimates of the two known Neptune-crossing Centaur binaries: Ceto/Phorcys ($\rho = 1.4$ g cm^{-3}; Grundy et al. 2007) and Typhon/Echidna ($\rho = 0.44$ g cm^{-3}; Grundy et al. 2008). This range of values is also consistent with the upper limit of Chiron's density of $\rho < 1.0$ g cm^{-3} as inferred by Meech et al. (1997). Figure 14 shows the escape velocity range of Chiron along with the value estimated by Braga-Ribas et al. (2023) with respect to measured dust grain velocities from outbursts by the JFC 67P/Churyumov–Gerasimenko (Grün et al. 2016; Agarwal et al. 2017; Rinaldi et al. 2018) and the Centaur 29P/Schwassman–Wachmann 1 (Miles 2016; Wierzchos & Womack 2020), which we use as a proxy for grain velocities on Chiron and list in Table 6.

As seen in Figure 14, most of the outbursts from comet 67P/Churyumov–Gerasimenko have dust grain velocities that do not exceed our estimated range of values for Chiron's escape velocity. While most of the grain velocities from the Centaur 29P/Schwassman–Wachmann 1 are much greater than Chiron's estimated escape velocity, the range of values from Wierzchos & Womack (2020) nevertheless overlaps with our range of estimated escape velocity values, including that of the shape model and density as reported by Braga-Ribas et al.
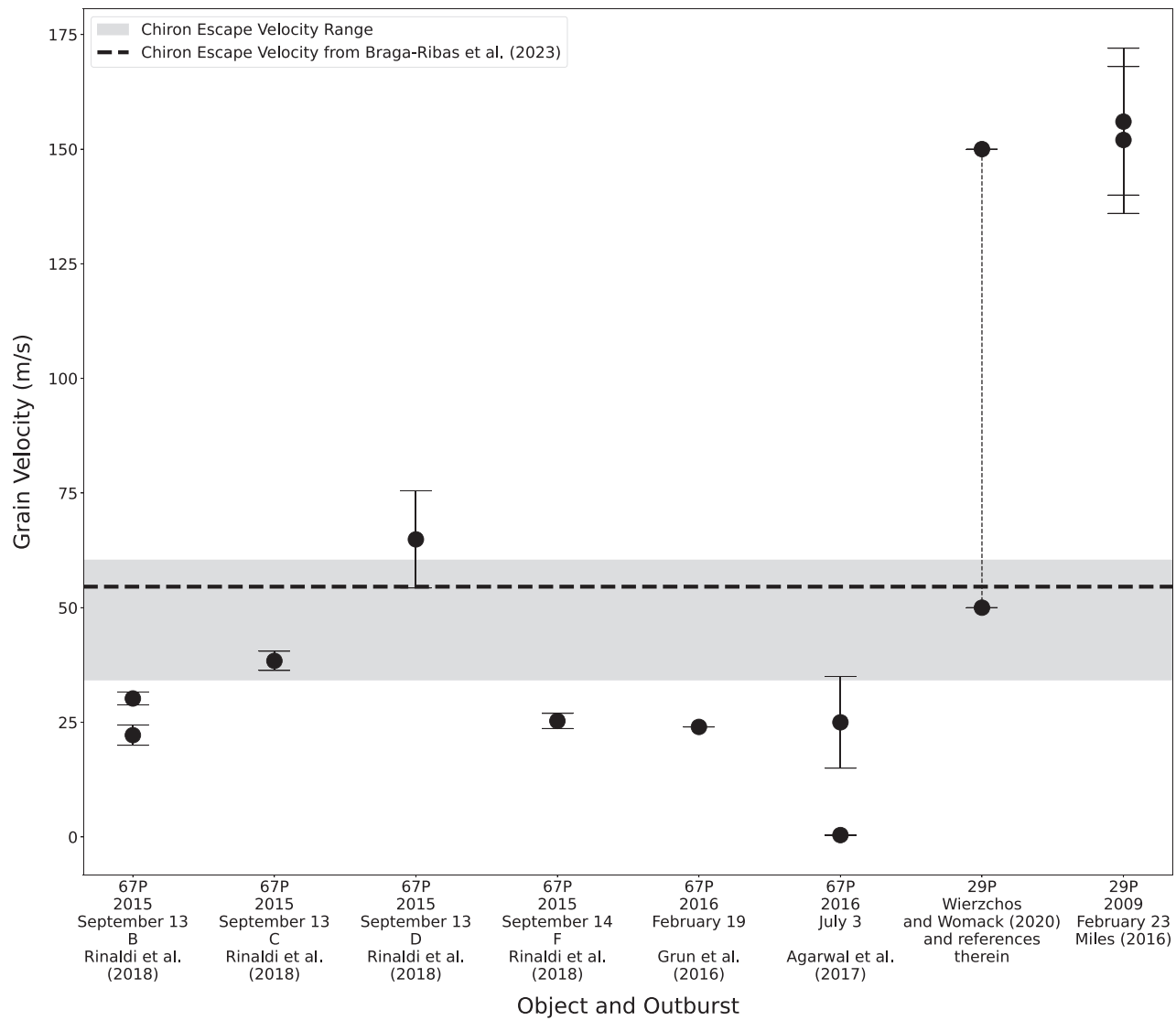
Figure 14. Dust grain velocity measurements of outbursts from the JFC 67P/Churuymov–Gerasimenko compared to the range of escape velocity values of Chiron (gray) estimated from known densities of Centaur binaries. The horizontal dashed black line indicates the value of Chiron's escape velocity according to the density estimate of Braga-Ribas et al. (2023).

Table 6
Comet 67P and 29P Dust Grain Velocities Used in This Analysis

Object	Date	Grain Velocity (m s^{-1})	Source
67P	2015 September 13 (Outburst B)	30.2 ± 1.4	Rinaldi et al. (2018)
67P	2015 September 13 (Outburst B)	22.2 ± 2.2	Rinaldi et al. (2018)
67P	2015 September 13 (Outburst C)	38.4 ± 2.0	Rinaldi et al. (2018)
67P	2015 September 13 (Outburst D)	64.9 ± 10.0	Rinaldi et al. (2018)
67P	2015 September 14 (Outburst F)	25.30 ± 1.65	Rinaldi et al. (2018)
67P	2016 February 19	24.0	Grün et al. (2016)
67P	2016 July 3	25.0 ± 10.0	Agarwal et al. (2017)
67P	2016 July 3	0.41 ± 0.05	Agarwal et al. (2017)
29P		50.00–150.00	Wierzchos & Womack (2020)
29P	2009 February 23	154 ± 18	Miles (2016)

(2023). Assuming these dust grain velocities to be representative of cometary activity on Chiron, this first-order comparison shows that an entirely bound coma is a plausible outcome of a cometary outburst. In this situation, any ejecta that remains bound to Chiron's nucleus may act to augment the ring system around the Centaur, and evidence of this activity may be detectable from differences in detected structures around Chiron in (future) occultation studies (Ortiz et al. 2023).

However, without accurate values of its nuclear escape velocity and dust grain velocities from its cometary outbursts, we cannot rule out the possibility that Chiron is exhibiting a spatially extended coma that is too faint to be observed at aphelion.

Chiron's heliocentric distance of 18.9 au at the time of the first observation of the 2021–2022 observing season places it far beyond the boundary of direct sublimation of surface water ice at ∼3 au (Meech & Svoren 2004; Womack et al. 2017), therefore ruling out this mechanism as being responsible for Chiron's 2021 epoch of cometary activity. Beyond this boundary, cometary activity in the solar system is thought to be dominated by the sublimation of the volatile species CO and CO_2 (A'Hearn et al. 2012; Ootsubo et al. 2012; Reach et al. 2013; Bauer et al. 2015; Cochran et al. 2015; Womack et al. 2017) and the transition of water ice from an amorphous to a crystalline configuration (Jewitt 2009; Guilbert-Lepoutre 2012; Li et al. 2020). Although Chiron resides at distances too close to the Sun for these species to be maintained on its surface (Jewitt 2009), subsurface pockets of these species could persist across the Centaur's lifetime before being exposed to insolation via surface disruption (Prialnik 1992). This is further corroborated by the findings of Birch & Umurhan (2024) that imply that large quantities of CO could be preserved in the interiors of small KBOs. An alternative mechanism proposed to explain activity throughout the Centaur population is the release of volatiles from the transition of subsurface water ice from an amorphous to a crystalline configuration caused by the propagation of the thermal wave through the object's interior (Jewitt 2009). Guilbert-Lepoutre (2012) found that this transition can occur for Centaurs at heliocentric distances up to 16 au. Though Chiron resided beyond this outer boundary during its 2021 Brightening Event, we cannot rule out Chiron being active in the years preceding the outburst, as evidenced from a possible detection of a tail-like feature by Cikota et al. (2018). Combined with the considerably different size of Chiron (volume-equivalent radius 98 km; Braga-Ribas et al. 2023) compared to the Centaur model of Guilbert-Lepoutre (2012; 50 km), this means we cannot rule out the amorphous-to-crystalline transition of water ice as being responsible for Chiron's 2021 Brightening Event. We therefore consider newly exposed pockets of volatile ices and the amorphous-to-crystalline water-ice transition to both be viable mechanisms for Chiron's 2021 Brightening Event.

6. Conclusions

We have analyzed a ∼1 mag brightening in reduced/apparent magnitude by the large Centaur Chiron that started in 2021, referred to in this study as the 2021 Brightening Event. Combining multifilter observations from multiple instruments, we find that from 2021 June to 2023 February, Chiron remained brighter than its pre-2021 Brightening Event magnitude and did not exhibit any significant change in color index across time. The ∼1 mag increase of Chiron's brightness and its continued brightening across the 2021–2022 observing season disfavors rotational modulation, solar phase angle effects, and seasonal albedo features as plausible causes for this behavior. We find that the Ortiz et al. (2015) model of Chiron's reported ring system also does not account for the observed brightening. Chiron's enhanced brightening followed by its slow dimming across its 2022–2023 observing season, combined with its duration according with that of previous

cometary outbursts, means we propose that the best explanation for the 2021 Brightening Event is an epoch of either new or increased cometary activity, caused either by the amorphous-to-crystalline water-ice transition or by newly exposed pockets of subsurface volatiles. We cannot completely rule out Chiron's ring system playing a role in its observed brightening, potentially by a collision of two small, unseen shepherd moons within the ring system, highlighting the need for further occultation observations over the coming years. We find no visible coma in any of our deep-stack Gemini images, yet brightness values of Chiron's historical comae imply that the Centaur could be exhibiting a coma that is too faint to be observed near aphelion or, alternatively, is bound to the nucleus.

We highlight that the multiyear baseline and high cadence of the ATLAS observations allowed Chiron's brightening to be detected and discerned via analysis of the Centaur's phase curve. The Rubin Observatory Legacy Survey of Space and Time (LSST) by the Vera C. Rubin Observatory (LSST Science Collaboration et al. 2009; Ivezić et al. 2019; Jurić et al. 2019; Schwamb et al. 2023) will allow a 10 yr data set of multifilter, high-cadence observations of approximately 5 million solar system objects, including the Centaur population (Guy et al. 2022). This will enable the discovery and analysis of potentially unseen Centaur activity via phase curve analysis for many more Centaurs. Our analysis thus serves as an example of how such a data set can be used to detect cometary activity exhibited by Centaurs, including Chiron, itself a possible flyby target for future space missions (Singer et al. 2019).

Facilities: ATLAS, PO:1.2m (ZTF), PS1, Blanco (DES), Gaia, LCOGT (1 m telescopes), TRAPPIST, Gemini Gillett.

Software: Astropy (Astropy Collaboration et al. 2013, 2018), BANZAI (McCully et al. 2018), CALVIACAT (Kelley & Lister 2021), ccdproc (Craig et al. 2017), DRAGONS (Labrie et al. 2019, 2023), Jupyter Notebook (Kluyver et al. 2016), math (Van Rossum 2020), Matplotlib (Hunter 2007), NEOExchange (Lister et al. 2021), Numpy (van der Walt et al. 2011; Harris et al. 2020), os (Van Rossum 2020), Pandas (pandas development team 2020), PHOTOMETRYPIPELINE (Mommert 2017), Photutils (Bradley 2023), python (https://www.python.org), SAOImageDS9 (Joye 2019), SciPy (Virtanen et al. 2020), SExtractor Python (Bertin & Arnouts 1996; Barbary 2016).

Appendix
Observations

All observations used in this study are listed in Tables A1–A8 below, separated by telescope/survey.

Table A1
ATLAS Observations of Chiron

MJD[a]	Magnitude	Magnitude Uncertainty	Filter	R_H[b]	Δ[c]	α[d]
				(au)	(au)	(deg)
57229.491001	17.945	0.141	*o*	18.150299	17.456002	2.3875
57229.493189	17.784	0.128	*o*	18.150300	17.455976	2.3874
57229.514768	17.899	0.083	*o*	18.150315	17.455723	2.3866
57229.541811	18.083	0.097	*o*	18.150333	17.455407	2.3855
57246.461081	18.565	0.103	*c*	18.161646	17.289222	1.6685
57246.466938	18.243	0.093	*c*	18.161649	17.289175	1.6682
57246.502626	18.597	0.122	*c*	18.161673	17.288894	1.6665
57313.399531	18.176	0.131	*c*	18.205515	17.402518	1.8983
57330.396038	18.073	0.153	*o*	18.216428	17.623558	2.5419
57356.286485	18.316	0.137	*o*	18.232879	18.049571	3.0602

Notes. All observation exposure times are 30 s.
[a] Modified Julian Date of observation, measured at midpoint of exposure.
[b] Heliocentric distance.
[c] Geocentric distance.
[d] Solar phase angle.

(This table is available in its entirety in machine-readable form in the online article.)

Table A2
ZTF Observations of Chiron

MJD[a]	Magnitude	Magnitude Uncertainty	Filter	R_H[b]	Δ[c]	α[d]
				(au)	(au)	(deg)
58789.206690	18.739	0.098	ZTF *g*	18.816841	18.019101	1.8359
58789.229294	18.311	0.061	ZTF *r*	18.816846	18.019345	1.8369
58828.127928	18.363	0.089	ZTF *r*	18.823712	18.583454	2.9246
58831.071377	18.369	0.065	ZTF *r*	18.824212	18.633899	2.9539
58855.191424	18.568	0.106	ZTF *r*	18.828206	19.051763	2.8959
58863.091262	18.463	0.073	ZTF *r*	18.829474	19.182602	2.7667
58863.121482	18.953	0.118	ZTF *g*	18.829479	19.183090	2.7661
59034.382199	18.407	0.094	ZTF *r*	18.852102	18.763725	3.0869
59038.378009	18.424	0.105	ZTF *r*	18.852518	18.697623	3.0678
59044.358461	18.774	0.120	ZTF *g*	18.853133	18.599799	3.0134

Notes. All observation exposure times are 30 s.
[a] Modified Julian Date of observation.
[b] Heliocentric distance.
[c] Geocentric distance.
[d] Solar phase angle.

(This table is available in its entirety in machine-readable form in the online article.)

Table A3
Pan-STARRS Observations of Chiron

MJD[a]	Magnitude	Magnitude Uncertainty	Filter	Exposure Time (s)	R_H[b] (au)	Δ[c] (au)	α[d] (deg)
54992.603300	17.5890	0.0324	y	30.0	15.852166	15.419669	3.3679
54992.615072	17.6314	0.0372	y	30.0	15.852182	15.419506	3.3676
55345.600003	17.7551	0.0448	y	30.0	16.322017	16.165605	3.5340
55345.612039	17.6574	0.0477	y	30.0	16.322033	16.165422	3.5339
55369.612051	17.6963	0.0205	z	30.0	16.352523	15.819741	3.0845
55439.437320	17.6177	0.0086	r	40.0	16.440162	15.450846	0.7197
55439.448968	17.6046	0.0084	r	40.0	16.440177	15.450896	0.7203
55441.438908	17.5285	0.0075	i	45.0	16.442651	15.460135	0.8237
55444.289450	18.0477	0.0106	g	43.0	16.446193	15.475389	0.9771
55444.301023	18.0487	0.0108	g	43.0	16.446207	15.475455	0.9777

Notes.
[a] Modified Julian Date of observation, measured at midpoint of exposure.
[b] Heliocentric distance.
[c] Geocentric distance.
[d] Solar phase angle.

(This table is available in its entirety in machine-readable form in the online article.)

Table A4
DES Observations of Chiron

MJD[a]	Magnitude	Magnitude Uncertainty	Filter	R_H[b] (au)	Δ[c] (au)	α[d] (deg)
56546.247289	18.2370	0.0042	g	17.618302	16.624231	0.5310
56951.130462	18.5977	0.0047	g	17.951314	17.224747	2.2170
56958.142839	18.1324	0.0176	Y	17.956625	17.319614	2.4769
57294.162942	17.9745	0.0140	Y	18.193055	17.236986	0.9678
57327.048550	18.1877	0.0043	i	18.214288	17.575397	2.4321
57327.049921	18.2352	0.0040	r	18.214289	17.575416	2.4321
57327.051287	18.6546	0.0046	g	18.214290	17.575435	2.4321
57657.141772	18.0368	0.0042	i	18.408731	17.426478	0.6410
57657.143145	18.1057	0.0040	r	18.408732	17.426484	0.6410
57657.144516	18.5195	0.0046	g	18.408732	17.426490	0.6411

Notes.
[a] Modified Julian Date of observation.
[b] Heliocentric distance.
[c] Geocentric distance.
[d] Solar phase angle.

(This table is available in its entirety in machine-readable form in the online article.)

Table A5
Gaia Observations of Chiron

MJD[a]	Magnitude	Magnitude Uncertainty	Filter	R_H[b]	Δ[c]	α[d]
				(au)	(au)	(deg)
56961.329590	18.4157	0.0077	Gaia *G*	17.959033	17.365889	2.5822
56961.329646	18.4157	0.0077	Gaia *G*	17.959033	17.365890	2.5823
56961.329702	18.4157	0.0077	Gaia *G*	17.959033	17.365890	2.5823
56961.329759	18.4157	0.0077	Gaia *G*	17.959033	17.365891	2.5823
56961.329815	18.4157	0.0077	Gaia *G*	17.959034	17.365892	2.5823
56961.329871	18.4157	0.0077	Gaia *G*	17.959034	17.365893	2.5823
56961.329927	18.4157	0.0077	Gaia *G*	17.959034	17.365894	2.5823
56961.329984	18.4157	0.0077	Gaia *G*	17.959034	17.365895	2.5823
56961.330040	18.4157	0.0077	Gaia *G*	17.959034	17.365896	2.5823
56961.403597	18.4020	0.0075	Gaia *G*	17.959089	17.366985	2.5846

Notes.
[a] Modified Julian Date of observation.
[b] Heliocentric distance.
[c] Geocentric distance.
[d] Solar phase angle.

(This table is available in its entirety in machine-readable form in the online article.)

Table A6
LOOK Observations of Chiron

MJD[a]	R_H[b]	Δ[c]	α[d]	Seeing	Filter	Exposure Time	Air Mass[e]	Magnitude	Magnitude Uncertainty
	(au)	(au)	(deg)	(arcsec)		(s)			
59463.320833	18.867587	17.971398	1.4368	1.73	*w*	245.0	1.344	17.802	0.044
59463.324306	18.867587	17.971371	1.4366	1.68	*w*	245.0	1.355	17.795	0.051
59463.327083	18.867587	17.971350	1.4365	1.62	*w*	245.0	1.367	17.771	0.042
59463.330556	18.867587	17.971323	1.4363	1.61	*w*	245.0	1.380	17.769	0.043
59827.018750	18.834124	17.981445	1.6770	1.92	*g'*	180.1	1.347	18.178	0.033
59827.020833	18.834124	17.981425	1.6769	2.06	*r'*	180.1	1.332	17.936	0.034
59827.023611	18.834124	17.981400	1.6768	2.01	*g'*	180.1	1.318	18.241	0.032
59827.025694	18.834123	17.981381	1.6767	1.71	*r'*	180.1	1.304	17.885	0.031
59840.381944	18.832074	17.882598	1.0286	2.09	*g'*	180.1	1.136	18.156	0.022
59840.386806	18.832073	17.882571	1.0284	2.10	*g'*	180.1	1.147	18.159	0.022

Notes.
[a] Modified Julian Date of observation.
[b] Heliocentric distance.
[c] Geocentric distance.
[d] Solar phase angle.
[e] Mean air mass of Chiron during exposure.

(This table is available in its entirety in machine-readable form in the online article.)

Table A7
TRAPPIST-South Observations of Chiron

MJD[a]	Magnitude	Magnitude Uncertainty	Filter	R_H[b]	Δ[c]	α[d]
				(au)	(au)	(deg)
56063.41221	17.960	0.055	R	17.152954	17.359322	3.2885
56063.41861	18.043	0.065	R	17.152960	17.359225	3.2886
56063.42314	18.312	0.066	V	17.152965	17.359156	3.2887
56063.42612	18.999	0.110	B	17.152968	17.359111	3.2887
56063.42901	17.976	0.064	R	17.152971	17.359067	3.2887
56063.43192	18.279	0.077	V	17.152974	17.359023	3.2888
56084.40271	18.336	0.111	V	17.174743	17.033325	3.3678
56084.41155	18.732	0.152	B	17.174753	17.033188	3.3678
56101.39035	17.866	0.050	R	17.192274	16.777463	3.1319
56101.39330	17.854	0.053	R	17.192277	16.777420	3.1319

Notes.
[a] Modified Julian Date of observation.
[b] Heliocentric distance.
[c] Geocentric distance.
[d] Solar phase angle.

(This table is available in its entirety in machine-readable form in the online article.)

Table A8
Gemini Observing Details and Photometry

MJD[a] Date	R_H[b]	Δ[c]	α[d]	Seeing	Filter	Total Exp. Time	Air Mass[e]	Magnitude	Magnitude Uncertainty
	(au)	(au)	(deg)	(arcsec)		(s)			
59446.57370	18.868	18.135	2.166	0.945	g	180	1.040	18.327	0.039
59446.57704	18.868	18.135	2.166	0.898	r	360	1.046	17.897	0.027
59446.58361	18.868	18.135	2.165	0.847	i	180	1.053	17.784	0.030
59521.38615	18.865	18.016	1.587	1.216	g	990	1.109	18.012	0.021
59521.40480	18.865	18.016	1.588	0.966	i	990	1.163	17.451	0.006
59557.31971	18.863	18.487	2.791	1.488	g	990	1.232	18.185	0.019
59557.33648	18.863	18.488	2.791	1.151	i	990	1.329	17.712	0.019
59754.58140	18.844	19.049	3.011	0.492	g	360	1.460	18.601	0.046
59754.58683	18.844	19.048	3.011	0.422	r	360	1.413	18.100	0.035
59793.50172	18.839	18.406	2.828	1.040	g	900	1.247	18.483	0.040
59793.51530	18.839	18.406	2.828	0.909	r	600	1.190	17.932	0.033
59793.52565	18.839	18.406	2.827	0.808	i	600	1.149	17.787	0.029

Notes.
[a] UTC at start of image sequence.
[b] Heliocentric distance.
[c] Geocentric distance.
[d] Solar phase angle.
[e] Mean air mass of Chiron during exposure.

ORCID iDs

Matthew M. Dobson ⓘ https://orcid.org/0000-0002-1105-7980

Megan E. Schwamb ⓘ https://orcid.org/0000-0003-4365-1455

Alan Fitzsimmons ⓘ https://orcid.org/0000-0003-0250-9911

Charles Schambeau ⓘ https://orcid.org/0000-0003-1800-8521

Aren Beck ⓘ https://orcid.org/0000-0002-5780-7062

Larry Denneau ⓘ https://orcid.org/0000-0002-7034-148X

Nicolas Erasmus ⓘ https://orcid.org/0000-0002-9986-3898

A. N. Heinze ⓘ https://orcid.org/0000-0003-3313-4921

Luke J. Shingles ⓘ https://orcid.org/0000-0002-5738-1612

Robert J. Siverd ⓘ https://orcid.org/0000-0001-5016-3359

Ken W. Smith ⓘ https://orcid.org/0000-0001-9535-3199

John L. Tonry ⓘ https://orcid.org/0000-0003-2858-9657

Henry Weiland ⓘ https://orcid.org/0000-0003-1847-9008

David. R. Young ⓘ https://orcid.org/0000-0002-1229-2499

Michael S. P. Kelley ⓘ https://orcid.org/0000-0002-6702-7676

Tim Lister ⓘ https://orcid.org/0000-0002-3818-7769

Pedro H. Bernardinelli ⓘ https://orcid.org/0000-0003-0743-9422

Marin Ferrais ⓘ https://orcid.org/0000-0002-0535-652X

Emmanuel Jehin ⓘ https://orcid.org/0000-0001-8923-488X

Grigori Fedorets ⓘ https://orcid.org/0000-0002-8418-4809

Susan D. Benecchi ⓘ https://orcid.org/0000-0001-8821-5927

Anne J. Verbiscer ⓘ https://orcid.org/0000-0002-3323-9304

Joseph Murtagh ⓘ https://orcid.org/0000-0001-9505-1131

René Duffard ⓘ https://orcid.org/0000-0001-5963-5850

Edward Gomez ⓘ https://orcid.org/0000-0001-5749-1507

Joey Chatelain ⓘ https://orcid.org/0000-0002-1278-5998

Sarah Greenstreet ⓘ https://orcid.org/0000-0002-4439-1539

References

Abbott, T. M. C., Adamów, M., Aguena, M., et al. 2021, ApJS, 255, 20

Agarwal, J., Della Corte, V., Feldman, P. D., et al. 2017, MNRAS, 469, s606

A'Hearn, M. F., Feaga, L. M., Keller, H. U., et al. 2012, ApJ, 758, 29

Astropy Collaboration, Price-Whelan, A. M., Sipőcz, B. M., et al. 2018, AJ, 156, 123

Astropy Collaboration, Robitaille, T. P., Tollerud, E. J., et al. 2013, A&A, 558, A33

Bagnulo, S., Boehnhardt, H., Muinonen, K., et al. 2006, A&A, 450, 1239

Bailey, B. L., & Malhotra, R. 2009, Icar, 203, 155

Barbary, K. 2016, JOSS, 1, 58

Bauer, J. M., Grav, T., Blauvelt, E., et al. 2013, ApJ, 773, 22

Bauer, J. M., Meech, K. J., Fernández, Y. R., et al. 2003, Icar, 166, 195

Bauer, J. M., Stevenson, R., Kramer, E., et al. 2015, ApJ, 814, 85

Bellm, E. C., Kulkarni, S. R., Graham, M. J., et al. 2019, PASP, 131, 018002

Belskaya, I. N., Bagnulo, S., Barucci, M. A., et al. 2010, Icar, 210, 472

Bernardinelli, P. & Dark Energy survey 2022, AAS Meeting Abstracts, 54, 332.07

Bernardinelli, P. H., Bernstein, G. M., Jindal, N., et al. 2023, ApJS, 269, 18

Bernardinelli, P. H., Bernstein, G. M., Sako, M., et al. 2020, ApJS, 247, 32

Bernardinelli, P. H., Bernstein, G. M., Sako, M., et al. 2022, ApJS, 258, 41

Bertin, E., & Arnouts, S. 1996, A&AS, 117, 393

Betzler, A. S. 2023, MNRAS, 523, 3678

Birch, S. P. D., & Umurhan, O. M. 2024, Icar, 413, 116027

Bradley, L. 2023, astropy/photutils: v1.8.0, Zenodo, doi:10.5281/zenodo.7946442

Braga-Ribas, F., Pereira, C. L., Sicardy, B., et al. 2023, A&A, 676, A72

Braga-Ribas, F., Sicardy, B., Ortiz, J. L., et al. 2014, Natur, 508, 72

Brown, T. M., Baliber, N., Bianco, F. B., et al. 2013, PASP, 125, 1031

Buie, M. W., Olkin, C., McDonald, S., et al. 1993, IAUC, 5898, 1

Buratti, B. J., & Dunbar, R. S. 1991, ApJL, 366, L47

Bus, S. J., A'Hearn, M. F., Bowell, E., & Stern, S. A. 2001, Icar, 150, 94

Bus, S. J., A'Hearn, M. F., Schleicher, D. G., & Bowell, E. 1991, Sci, 251, 774

Bus, S. J., Bowell, E., Harris, A. W., & Hewitt, A. V. 1989, Icar, 77, 223

Bus, S. J., Buie, M. W., Schleicher, D. G., et al. 1996, Icar, 123, 478

Chambers, K. C., Magnier, E. A., Metcalfe, N., et al. 2016, arXiv:1612.05560

Choi, Y. J., Weissman, P., Chesley, S., et al. 2006a, CBET, 563, 1

Choi, Y. J., Weissman, P. R., & Polishook, D. 2006b, IAUC, 8656, 2

Cikota, S., Fernández-Valenzuela, E., Ortiz, J. L., et al. 2018, MNRAS, 475, 2512

Cochran, A. L., Levasseur-Regourd, A.-C., Cordiner, M., et al. 2015, SSRv, 197, 9

Craig, M., Crawford, S., Seifert, M., et al. 2017, astropy/ccdproc: v1.3.0.post1, Zenodo, doi:10.5281/zenodo.1069648

Dahlgren, M., Fitzsimmons, A., Lagerkvist, C. I., & Williams, I. P. 1990, in Nordic-Baltic Astronomy Meeting, ed. C. I. Lagerkvist, D. Kiselman, & M. Lindgren (Uppsala: Uppsala Universiter), 83

Dahlgren, M., Lagerkvist, C. I., Fitzsimmons, A., & Williams, I. P. 1991, MNRAS, 250, 115

Denneau, L., Jedicke, R., Grav, T., et al. 2013, PASP, 125, 357

Devogèle, M., Ferrais, M., Jehin, E., et al. 2021, MNRAS, 505, 245

Di Sisto, R. P., & Brunini, A. 2007, Icar, 190, 224

Dobson, M. M., Schwamb, M. E., Fitzsimmons, A., et al. 2021, RNAAS, 5, 211

Dobson, M. M., Schwamb, M. E., Benecchi, S. D., et al. 2023, PSJ, 4, 75

Duffard, R., Lazzaro, D., Pinto, S., et al. 2002, Icar, 160, 44

Duncan, M., Levison, H., & Dones, L. 2004, in Comets II, ed. M. C. Festou, H. U. Keller, & H. A. Weaver (Tucson, AZ: Univ. Arizona Press), 193

Duncan, M. J., & Levison, H. F. 1997, Sci, 276, 1670

Elliot, J. L., Olkin, C. B., Dunham, E. W., et al. 1995, Natur, 373, 46

Feldman, P. D., Cochran, A. L., & Combi, M. R. 2004, in Comets II, ed. M. C. Festou, H. U. Keller, & H. A. Weaver (Tucson, AZ: Univ. Arizona Press), 425

Fernández, J. A., Helal, M., & Gallardo, T. 2018, P&SS, 158, 6

Fernández, Y. R., Kelley, M. S., Lamy, P. L., et al. 2013, Icar, 226, 1138

Finkbeiner, D. P., Schlafly, E. F., Schlegel, D. J., et al. 2016, ApJ, 822, 66

Flaugher, B., Diehl, H. T., Honscheid, K., et al. 2015, AJ, 150, 150

Flewelling, H. A., Magnier, E. A., Chambers, K. C., et al. 2020, ApJS, 251, 7

Fornasier, S., Lellouch, E., Müller, T., et al. 2013, A&A, 555, A15

Gaia Collaboration, Prusti, T., de Bruijne, J. H. J., et al. 2016, A&A, 595, A1

Gaia Collaboration, Spoto, F., Tanga, P., et al. 2018, A&A, 616, A13

Gaia Collaboration, Vallenari, A., Brown, A. G. A., et al. 2023, A&A, 674, A1

Galiazzo, M., de la Fuente Marcos, C., de la Fuente Marcos, R., et al. 2016, Ap&SS, 361, 212

Gimeno, G., Roth, K., Chiboucas, K., et al. 2016, Proc. SPIE, 9908, 99082S

Graham, M. J., Kulkarni, S. R., Bellm, E. C., et al. 2019, PASP, 131, 078001

Groussin, O., Lamy, P., & Jorda, L. 2004, A&A, 413, 1163

Grün, E., Agarwal, J., Altobelli, N., et al. 2016, MNRAS, 462, S220

Grundy, W. M., Noll, K. S., Virtanen, J., et al. 2008, Icar, 197, 260

Grundy, W. M., Stansberry, J. A., Noll, K. S., et al. 2007, Icar, 191, 286

Guilbert-Lepoutre, A. 2012, AJ, 144, 97

Guy, L. P., Cuillandre, J.-C., Bachelet, E., et al. 2022, Rubin-Euclid Derived Data Products – Initial Recommendations, Version 1.1, Zenodo, doi:10.5281/zenodo.5836022

Gwyn, S. D. J., Hill, N., & Kavelaars, J. J. 2012, PASP, 124, 579

Hahn, G., & Bailey, M. E. 1990, Natur, 348, 132

Harris, C. R., Millman, K. J., van der Walt, S. J., et al. 2020, Natur, 585, 357

Hartmann, W. K., Tholen, D. J., Meech, K. J., & Cruikshank, D. P. 1990, Icar, 83, 1

Hodapp, K. W., Kaiser, N., Aussel, H., et al. 2004, AN, 325, 636

Hook, I. M., Jørgensen, I., Allington-Smith, J. R., et al. 2004, PASP, 116, 425

Hunter, J. D. 2007, CSE, 9, 90

Ivezić, Ž, Kahn, S. M., Tyson, J. A., et al. 2019, ApJ, 873, 111

Jaeger, M., Prosperi, E., Vollmann, W., et al. 2011, IAUC, 9213, 2

James, N. D. 2018, JBAA, 128, 51

Jehin, E., Gillon, M., Queloz, D., et al. 2011, Msngr, 145, 2

Jester, S., Schneider, D. P., Richards, G. T., et al. 2005, AJ, 130, 873

Jewitt, D. 2009, AJ, 137, 4296

Jewitt, D. 2015, AJ, 150, 201

Jordi, C., Gebran, M., Carrasco, J. M., et al. 2010, A&A, 523, A48

Joye, W. 2019, SAOImageDS9/SAOImageDS9 v8.0.1, Zenodo, doi:10.5281/zenodo.2530958

Jurić, M., Jones, R. L., Bryce Kalmbach, J., et al. 2019, arXiv:1901.08549

Kaiser, N. 2004, Proc. SPIE, 5489, 11

Kaiser, N., Aussel, H., Burke, B. E., et al. 2002, Proc. SPIE, 4836, 154

Kareta, T., Sharkey, B., Noonan, J., et al. 2019, AJ, 158, 255

Kelley, M., & Lister, T. 2021, mkelley/calviacat: v1.2.0, Zenodo, doi:10.5281/zenodo.5061298

Kluyver, T., Ragan-Kelley, B., Pérez, F., et al. 2016, in Positioning and Power in Academic Publishing: Players, Agents and Agendas, ed. F. Loizides & B. Scmidt (IOS Press), 87

Labrie, K., Anderson, K., Cárdenes, R., Simpson, C., & Turner, J. E. H. 2019, in ASP Conf. Ser. 523, Astronomical Data Analysis Software and Systems XXVII, ed. P. J. Teuben et al. (San Francisco, CA: ASP), 321

Lazzaro, D., Florczak, M. A., Angeli, C. A., et al. 1997, P&SS, 45, 1607

Labrie, K., Simpson, C., Cardenes, R., et al. 2023, RNAAS, 7, 214

Lazzaro, D., Florczak, M. A., Betzler, A., et al. 1996, P&SS, 44, 1547

Levison, H. F., & Duncan, M. J. 1997, Icar, 127, 13

Li, J., Jewitt, D., Mutchler, M., Agarwal, J., & Weaver, H. 2020, AJ, 159, 209

Lilly, E., Hsieh, H., Bauer, J., et al. 2021, PSJ, 2, 155

Lilly, E., Jevčák, P., Schambeau, C., et al. 2024, ApJL, 960, L8

Lister, T., Kelley, M. S. P., Holt, C. E., et al. 2022, PSJ, 3, 173

Lister, T. A., Gomez, E., Chatelain, J., et al. 2021, Icar, 364, 114387

Lowry, S. C., & Fitzsimmons, A. 2005, MNRAS, 358, 641

LSST Science Collaboration, Abell, P. A., Allison, J., et al. 2009, arXiv:0912.0201

Luu, J. X. 1993, PASP, 105, 946

Luu, J. X., & Jewitt, D. C. 1990, AJ, 100, 913

Magnier, E. A., Chambers, K. C., Flewelling, H. A., et al. 2020a, ApJS, 251, 3

Magnier, E. A., Sweeney, W. E., Chambers, K. C., et al. 2020b, ApJS, 251, 5

Magnier, E. A., Schlafly, E. F., Finkbeiner, D. P., et al. 2020c, ApJS, 251, 6

Marcialis, R. L., & Buratti, B. J. 1993, Icar, 104, 234

McCully, C., Volgenau, N. H., Harbeck, D.-R., et al. 2018, Proc. SPIE, 10707, 107070K

McCully, C., Crawford, S., Kovacs, G., et al. 2018, astropy/astroscrappy: v1.0.5 Zenodo Release, v1.0.5, Zenodo, doi:10.5281/zenodo.1482019

Meech, K. J. 1990, IAUC, 4947, 3

Meech, K. J., & Belton, M. J. S. 1989, IAUC, 4770, 1

Meech, K. J., & Belton, M. J. S. 1990, AJ, 100, 1323

Meech, K. J., Buie, M. W., Samarasinha, N. H., Mueller, B. E. A., & Belton, M. J. S. 1997, AJ, 113, 844

Meech, K. J., & Svoren, J. 2004, in Comets II, ed. M. C. Festou, H. U. Keller, & H. A. Weaver (Tucson, AZ: Univ. Arizona Press), 317

Melita, M. D., Duffard, R., Ortiz, J. L., & Campo-Bagatin, A. 2017, A&A, 602, A27

Miles, R. 2016, Icar, 272, 387

Möller, A., Peloton, J., Ishida, E. E. O., et al. 2021, MNRAS, 501, 3272

Mommert, M. 2017, A&C, 18, 47

Ootsubo, T., Kawakita, H., Hamada, S., et al. 2012, ApJ, 752, 15

Ortiz, J. L., Duffard, R., Pinilla-Alonso, N., et al. 2015, A&A, 576, A18

Ortiz, J. L., Pereira, C. L., Sicardy, B., et al. 2023, A&A, 676, L12

pandas development team 2020, pandas-dev/pandas: Pandas, latest, Zenodo, doi:10.5281/zenodo.3509134

Peixinho, N., Thirouin, A., Tegler, S. C., et al. 2020, in The Trans-Neptunian Solar System, ed. D. Prialnik, M. A. Barucci, & L. Young (Amsterdam: Elsevier), 307

Prialnik, D. 1992, ApJ, 388, 196

Reach, W. T., Kelley, M. S., & Vaubaillon, J. 2013, Icar, 226, 777

Rinaldi, G., Bockelée-Morvan, D., Ciarniello, M., et al. 2018, MNRAS, 481, 1235

Romon-Martin, J., Delahodde, C., Barucci, M. A., de Bergh, C., & Peixinho, N. 2003, A&A, 400, 369

Rousselot, P., Korsun, P. P., Kulyk, I., Guilbert-Lepoutre, A., & Petit, J. M. 2016, MNRAS, 462, S432

Ruprecht, J. D., Bosh, A. S., Person, M. J., et al. 2015, Icar, 252, 271

Sarid, G., Volk, K., Steckloff, J. K., et al. 2019, ApJL, 883, L25

Schleicher, D. 2010, Composite Dust Phase Function for Comets, Lowell Minor Planet Services, https://asteroid.lowell.edu/comet/dustphase/details

Schambeau, C. A., Fernández, Y. R., Samarasinha, N. H., Mueller, B. E. A., & Woodney, L. M. 2017, Icar, 284, 359

Schambeau, C. A., Fernández, Y. R., Samarasinha, N. H., Woodney, L. M., & Kundu, A. 2019, AJ, 158, 259

Schwamb, M. E., Jones, R. L., Yoachim, P., et al. 2023, ApJS, 266, 22

Seccull, T., Fraser, W. C., Puzia, T. H., Fitzsimmons, A., & Cupani, G. 2019, AJ, 157, 88

Shingles, L., Smith, K. W., Young, D. R., et al. 2021, TNSAN, 7, 1

Sickafoose, A. A., Levine, S. E., Bosh, A. S., et al. 2023, PSJ, 4, 221

Silva, A. M., & Cellone, S. A. 2001, P&SS, 49, 1325

Singer, K. N., Stern, S. A., Stern, D., Verbiscer, A., & Olkin, C. 2019, EPSC-DPS Joint Meeting, 2019, EPSC–DPS2019–2025

Smith, K. W., Smartt, S. J., Young, D. R., et al. 2020, PASP, 132, 085002

Sykes, M. V., & Walker, R. G. 1991, Sci, 251, 777

Tanga, P., Pauwels, T., Mignard, F., et al. 2023, A&A, 674, A12

The Dark Energy Survey Collaboration 2005, arXiv:astro-ph/0510346

Tholen, D. J., Hartmann, W. K., Cruikshank, D. P., et al. 1988, IAUC, 4554, 2

Tiscareno, M. S., & Malhotra, R. 2003, AJ, 126, 3122

Tonry, J. L., Denneau, L., Flewelling, H., et al. 2018b, ApJ, 867, 105

Tonry, J. L., Denneau, L., Heinze, A. N., et al. 2018a, PASP, 130, 064505

Tonry, J. L., Stubbs, C. W., Lykke, K. R., et al. 2012, ApJ, 750, 99

Trigo-Rodríguez, J. M., García-Melendo, E., Davidsson, B. J. R., et al. 2008, A&A, 485, 599

van der Walt, S., Colbert, S. C., & Varoquaux, G. 2011, CSE, 13, 22

van Dokkum, P. G. 2001, PASP, 113, 1420

Van Rossum, G., 2020 The Python Library Reference, release 3.8.2 (Python Software Foundation), https://www.python.org/downloads/release/python-382/

Virtanen, P., Gommers, R., Oliphant, T. E., et al. 2020, NatMe, 17, 261

Volk, K., & Malhotra, R. 2008, ApJ, 687, 714

Waters, C. Z., Magnier, E. A., Price, P. A., et al. 2020, ApJS, 251, 4

West, R. M. 1990, IAUC, 4970, 1

West, R. M. 1991, A&A, 241, 635

Wierzchos, K., & Womack, M. 2020, AJ, 159, 136

Willmer, C. N. A. 2018, ApJS, 236, 47

Womack, M., Sarid, G., & Wierzchos, K. 2017, PASP, 129, 031001